Characterisation of the Surface and Structural Properties of Gamma Ray and Electron Beam Irradiated Low Density Polyethylene

Kieran A. Murray[1], James E. Kennedy[1], Brian McEvoy[2], Olivier Vrain[2], Damien Ryan[2], Richard Cowman[2], Clement L. Higginbothama[1] *

[1]Materials Research Institute, Athlone Institute of Technology, Dublin Road, Athlone, Co. Westmeath, Ireland.

[2]Synergy Health Applied Sterilisation Technologies, IDA Business & Technology Park, Sragh, Tullamore, Co. Offaly, Ireland.

[1]kmurray@research.ait.ie; [2] jkennedy@ait.ie; [3]Brian.Mcevoy@synergyhealthplc.com; [4]Olivier.Vrain@synergyhealthplc.com; [5]Damien.Ryan@synergyhealthplc.com; [6]Richard.Cowman@synergyhealthplc.com;[7]chigginbotham@ait.ie

Abstract

It is of vital importance that most medical devices are sterilised prior to use. However, sterilisation performed by ionising radiation can cause significant damage and degradation to polymers due to the energetic secondary electrons released from the primary irradiation event. In this present work, low density polyethylene (LDPE) was subjected to a commercial gamma irradiator and a high energy electron beam irradiator (combined 10/12MeV unit, 30KW). Characterisation was performed on the non-irradiated and irradiated LDPE samples by several analytical methods. X-ray diffraction (XRD) revealed that the percentage crystallinity and crystalline size had no significant alterations. Scanning electron microscope (SEM) imagery illustrated a rougher sample surface subsequent to electron beam irradiation at 400kGy which was perhaps attributed to oxidative degradation. In addition, the fracture behaviour of the cryofractured surface specimens was highly influenced by electron beam irradiation. Colorimetry was employed in quantifying the effects of electron beam and gamma ray processing on the colour changes of LDPE. This technique identified that the gamma ray process leads to more discolouration of the LDPE material, indicating that the electron beam process was more user friendly.

Keywords

Electron beam irradiation; gamma irradiation; crystallinity; contact angle; colour measurement; low density polyethylene

Introduction

Crosslinking of low density polyethylene (LDPE) without the addition of crosslinking agents or other special additives can be achieved by exposing the material to various forms of radiation such as electron beam and gamma ray (Sharif, Aziz, & Hashim, 2000). This has potential commercial use due to property improvements where 3D crosslink networks form between polymeric chains which in turn could enhance thermal and chemical resistance and mechanical characteristics. Radiation crosslinking results in a product with properties that are similar or identical to those obtained by the chemical crosslinking process (Chodák, 1998; Salovey, 1962; Yan, Luo, & Jiang, 1993). Radiation crosslinking occurs quickly, therefore producing higher throughput. Another advantage of this process consists of the possibility of generating active intermediates in the solid polymer within a large temperature interval (Khonakdar, Jafari, Wagenknecht, & Jehnichen, 2006). However, ionising irradiation can result in adverse effects on material properties by promoting degradation affects. Yet the balance of crosslinking and scission reactions in polyolefin chains exposed to radiation processes that produce free radicals can perhaps result in sought after properties and new applications (Smedberg, Hjertberg, & Gustafsson, 1997; Suarez, da Costa Monteiro, & Mano, 2002; Viksne, Zicans, Kalkis, & Bledzki, 1997). Radiation initiates scission of C-C and C-H bonds leading to the formation of alkyl radicals (Kurtz, 2004) which are required to form chemically crosslinked 3D structure of covalent bonds between adjacent chain molecules. In addition, these free radicals can result in recombination processes (Göschel & Ulrich, 2009). The alkyl and the allyl radicals are the predominant free radicals produced by radiation in polyethylene (Dole, 1972). Radicals are also the reason for discolouration in some materials. This is due to the radicals produced

by irradiation which react with the oxygen diffusing through the material causing bleaching of the radical based colour centres (Clough, Gillen, Malone, & Wallace, 1996). Temperature plays a significant role in radiation induced reactions as a rise in 10°C doubles the reaction rates, therefore when polyethylene is exposed to 1 kilogray, the temperature of the material increases by 0.43°C (Berejka & Cleland, 2011). A thorough description of the numerous initiation procedures along with the mechanisms for these processes and specific features of each procedure was given in comprehensive reviews from Bhattacharya (2000) and Lazar, Rado & Rychlý (1990).

The current investigation is focused on another strategy, not explored up until now to the best of our knowledge. This aims at quantifying the effects of electron beam (combined 10/12MeV unit, 30KW) and gamma ray processing on the colour changes of LDPE while utilising two commercial processes. In addition, the percentage crystallinity obtained in previous results by MDSC (Murray et al., 2012), was compared to the percentage crystallinity values obtained from the XRD characterisation technique. This identified the relationship between both processes and determined whether the values fall into a similar range. SEM was performed on the surface of the non-irradiated and irradiated LDPE material to determine surface modifications induced by irradiation. Finally, goniometry was conducted on the surface of the non-irradiated and irradiated LDPE material by the sessile drop method. This distinguished the effects of irradiation on the hydrophilicity of the material.

Experimental

Material

This study was conducted using virgin low density polyethylene manufactured by ExxonMobil Chemical Company (Houston, USA). The material was supplied by the National Chemical Company, Ireland. Melt flow index (MFI) of the material was 0.55g/10min under loading of 2.16kg at 190°C, while the density was 0.929g/cm^{3}and had a melt temperature of 114°C.

Injection moulding and packaging

An Arburg injection moulding machine was utilised in manufacturing type IV ASTM (American society for testing and materials) D638 testing specimens with the use of LDPE material. Sample preparation played a significant role in the electron beam process as this controlled the uniformity of the irradiation dose on the samples. Each of the samples i.e. tensile specimens, and impact bars were placed into sealable LDPE bags in order to contain them in a controlled environment. Sample size, density, weight and orientation remained identical for each bag during the packaging process to facilitate uniform irradiation (Murray et al., 2013b).

Electron beam irradiation

Firstly, dose mapping was conducted on the LDPE testing specimens to determine the maximum and minimum dose zones and process reproducibility. A Mevex high energy electron beam irradiator (combined 10/12MeV unit, 20KW) was used to irradiate the samples at doses of 25, 50, 75, 100, 150, 200 and 400kGy. The dose rate was approximately 12.5kGy per pass on each side to accomplish a uniform irradiation dose. All samples were irradiated at room temperature in the presence of air at the Synergy Health plant (Tullamore, Ireland). The non-irradiated samples served as the baseline for each of the results obtained from the characterisation techniques.

Gamma ray irradiation

Gamma radiation was carried out on the LDPE samples with dose rates of 25 and 200 kGy. In order to attain accurate results, the samples were packaged and labelled identically, according to the samples for electron beam processing. A commercial gamma irradiator using a cobalt 60 energy source was used at the Synergy Health facility, Westport, Co. Mayo. The process was also performed in an air atmosphere.

X-Ray Diffraction

X-ray diffraction of all batches was examined via a Bruker AXS D8 Discover X-ray diffractometer. This characterisation technique was employed to investigate the modifications induced by irradiation such as crystallite size and relative crystallinity. All samples were positioned onto the sample loading plate located in the XRD chamber. During setup, the loading plate was set to oscillation mode (x,y axis movement) with an amplitude of 0.5mm. The value of 2θ ranged from 5 to 35°. The GADDS and Eva software was used to analyse the recorded results. By implementing Bragg's law, the d-spacing was determined from the XRD pattern. The d-spacing that depends on the angular position theta can be derived from equation 1(Suryanarayana & Norton, 1998).

$$n\lambda = 2d\sin\theta \qquad \text{Equation 1}$$

Where: n = Reflection order (1,2,3....)

λ = X-Ray wavelength

d = d-spacing

θ = Diffraction angle

Results from the experiment was analysed and the crystalline size was derived from the following equation (Niemantsverdriet, 2007; L. Singh & Singh, 2004):

$$\chi = \frac{K\lambda}{\beta \cos\theta} x \frac{180}{\pi} \qquad \text{Equation 2}$$

Where:

k = Scherrer constant or shape factor (e.g. **0.94** for cubic particles)

λ = Wavelength

θ = Incident angle (Half the 2 theta value)

β = Peak width (°)

Scanning Electron Microscope (SEM)

Surface morphologies of the non-irradiated and irradiated LDPE samples were investigated with the aid of a SEM. All test specimens were placed on special sample holders and then sputter coated with gold using a Beltec SCD 005 sputter coater prior to testing. A Mira FE SEM was used in high vacuum mode with an acceleration voltage of 10kV, a resolution of 100μm and a magnification of 388 x. (Murray et al., 2013a)

Goniometry

The contact angle was measured while operating an FTA (First Ten Angstroms, Virginia) 1000 machine. Each sample was measured three times in the same order to obtain a consistent value while using the sessile drop method. For contact angle measurements, a 0.002ml droplet of distilled water was ejected out of the micrometer syringe (GS-1200) onto the sample while using a 27 gauge needle. Images of the droplet on the surface of the sample were taken over a period of approximately 20 seconds and the FTA software was used to investigate the outcome result.

Colorimetry

Yellowness index was carried out according to ASTM D 1925 using a Lovibond RT600 sphere spectrophotometric colorimeter. Calibration was conducted on the instrument prior to testing by means of a calibration unit that was provided with the equipment (L = 94.91, a -1.01, b = +0.09). Five tests were measured from each sample of the different dose ranges. Each test performed on the non-irradiated and irradiated (electron beam and gamma ray) PEBA samples provided values for Hunter L (black (0) to white (100)), Hunter a (green (-) to red (+)) and Hunter b (blue (-) to yellow (+)).The overall colour difference was established by implementing statistical analysis of the ΔE values for L, a, and b. ΔE was calculated by using the following formula (Perera, Albano, González, Silva, & Ichazo, 2004):

$$\Delta E = \sqrt{(\Delta L)^2 + (\Delta a)^2 + (\Delta b)^2} \qquad \text{Equation 3}$$

ΔE is expressed as the difference between the control sample and the irradiated sample colour values.

Results and discussion

X-Ray Diffraction

To determine the effects of crosslinking on the crystalline structure and the degree of crystallinity of the irradiated LDPE material, XRD analysis was conducted. From the XRD pattern illustrated in Fig. 1, it is clear that the virgin material is semicrystalline in nature due to the peak at 21.65° (2θ) (R. Singh, Samra, Kumar, & Singh, 2008). The XRD patterns of various irradiated LDPE samples are presented in Fig. 1while the parameters are provided in Table 1. Three crystalline peaks appeared during this experiment at 21.5°, 24.3° and 36.5°. The orthorhombic phase for the peak located at 21.5° is 110, for peak 24.3° it is 200 and for peak 36.5° it is 210. These phases represent the diffraction angle which corresponds to the orthorhombic crystallite plane.

It is apparent that the peaks are not increasing according to the increase in irradiation dose as can be seen from the peak at a 2θ value of 21.5° in Fig. 1. The larger the crystals are of a given component, the sharper are the peaks on the XRD pattern for each crystal plane. As a result, the breadth of the peak can be related to the crystal size. The 150kGy sample had a remarkable increase in intensity at 21.5° from 793 (0kGy) to 1156.41 (150kGy). Scherrer equation (L. Singh & Singh, 2004) was utilised to calculate the crystalline size, whilst the GADDS software was employed to calculate the percentage crystallinity after the XRD experiment. Based on the results obtained in Table 1, it can be anticipated that upon irradiation there is only a slight change in both the percentage crystallinity and the crystalline size. This provides evidence that the electron beam irradiation mainly causes crosslinking to occur in the amorphous region

of the LDPE material. When the percentage crystallinity determined by XRD was compared to the percentage crystallinity of the MDSC experiment (Murray, et al., 2012), it was evident that the results were similar.

Scanning Electron Microscope (SEM)

In this study, four samples of the LDPE material were tested in order to identify changes induced by the electron beam irradiation process which are displayed in Fig. 2a-d. Two methods were implemented in order to discover these changes.

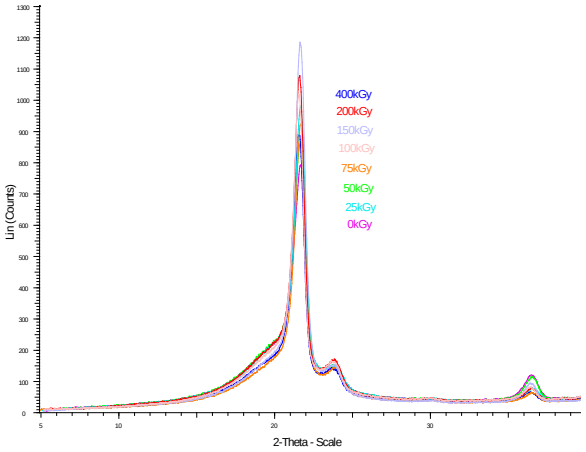

FIG. 1. XRD DIFFRACTOGRAM OF THE NON-IRRADIATED AND ELECTRON BEAM IRRADIATED LDPE IN THE 2Θ RANGE OF 5.2 - 40°

TABLE I XRD PARAMETERS OF THE NON-IRRADIATED AND ELECTRON BEAM IRRADIATED LDPE SAMPLES

Irradiation Dose (kGy)	2θ (deg.)	FWHM (deg.)	Crystallite Size L (Å)	XRD % Crystallinity	MDSC % Crystallinity
0	21.54	1.093	79	25.50	28.83
25	21.60	1.104	77	27.86	28.13
50	21.52	1.079	78	26.21	28.36
75	21.55	1.054	80	27.04	28.49
100	21.53	1.059	80	28.68	28.61
150	21.58	1.039	81	29.90	26.47
200	21.57	1.004	84	29.49	27.04
400	21.57	1.081	78	26.72	27.33

The first method involved testing the surface of the pristine (0kGy) and irradiated (400kGy) tensile specimens with an SEM at a magnification of 1.44kx. Before the test was conducted, each of the samples was placed on the pin mount adapter and then sputter coated in gold to enhance imagery during the experiment. The second method incorporated the investigation of freeze fractured (cryofracture) LDPE surfaces, before and after irradiation. This experiment included the testing of the 0 and 200kGy samples by use of SEM with a magnification of 388x. Previous to testing, the two samples (ASTM impact bars) were placed in liquid nitrogen for 20mins before being fractured by the charpy impact machine. LDPE is a flexible material by nature and would not break otherwise, thus liquid nitrogen was exploited to ensure that the polymer chains were completely frozen so as to achieve a high quality break. Both samples were left to one side after fracture, until they reached room temperature again. The samples were then prepared for SEM, by ensuring that the orientation of the fractured side was correctly placed on the pin mount adapter. Furthermore, they were sputter coated with gold to enhance imagery during the experiment. Surface changes (roughness changes) can be observed in a qualitative approach by the use of SEM imagery on each of the samples.

Image Fig. 2a (non-irradiated) displays a rough surface which appears to be blister like, while the irradiated (400kGy) sample at Fig.2 b demonstrates a smoother surface. This could be related to the formation of oxidation degradation on the surface of the LDPE material which in turn modifies the surface characteristics. In a previous study, Fourier transform infrared spectroscopy (FTIR) revealed that oxidative products were mainly found on the surface of LDPE (Murray, et al., 2012). Oxidative degradation caused by irradiation in air is a diffusion controlled process (Suarez & Mano, 2001), consequently, it affects mainly the surface layers and mechanical properties of irradiated polymers.

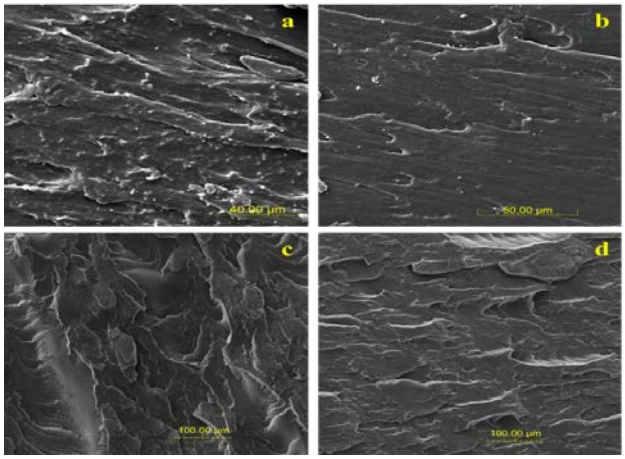

FIG. 2 (A) SEM IMAGE OF LDPE 0KGY AT 1.44KX FOR SURFACE OF TENSILE SPECIMEN (B) SEM IMAGE OF LDPE 400KGY AT 1.44KX FOR SURFACE OF TENSILE SPECIMEN (C) SEM IMAGE OF LDPE 0KGY AT 388X FOR SURFACE OF FRACTURED IMPACT BAR (D) SEM IMAGE OF LDPE 200KGY AT 388X FOR SURFACE OF FRACTURED IMPACT BAR

The effects of irradiation on the texture of the fractured surfaces are clearly defined by the images illustrated in Fig. 2c and d. Both samples can be characterised as a brittle fracture due to the glassy appearance and the presence of sharp fracture edges. A cleaner break is evident from image Fig. 2d which is perhaps due to the occurrence of crosslinking after irradiation exposure inducing fragility. The flaky/scaly appearance of both fractured samples could be attributed to damage caused by the intersection of microscopic crack branches with the main fractures produced during the impact (Carlos Miguez Suarez & Biasotto Mano, 2000; Lustiger & Corneliussen, 1987). Based on this study it was apparent that electron beam irradiation had a strong influence on the fracture behaviour. In addition, the surface characteristics were modified due to radiation degradation which is apparent from images a and b in Fig. 2.

Goniometry

The extent of hydrophilic modification of the electron beam radiation modified LDPE samples was investigated by contact angle measurements. Hydrophilicity gives a material a tendency to attract water to its surface, hence absorbing the water. The contact angle method used in this experiment was the sessile drop, which is the most widely used technique. Contact angle measurements were performed by calculating the angle formed between the surface of the solid and the line which was tangent to the droplet radius from the point of contact with the solid. When the contact angle has a value of zero, it results in wetting, whilst if the angle is between 0 and 90°, it results in the spreading of the water across the material surface. If the contact is between 0 and 90°, the material can be classified as hydrophilic due to the molecular attraction. However, if the contact angle is greater than 90°, the material can be classified as a hydrophobic material. This results in the water 'balling-up' hence, causing it to run of the surface easily (Dadbin, 2002; Garbassi, Morra, & Occhielo, 1996).

Fig. 3 illustrates the variation of the contact angle measurements of LDPE samples for different irradiation dose rates. Different values have been reported for the contact angle of untreated LDPE from the literature depending on the procedure and samples used. A value of 87° was given from research work which entailed modifying various polymers using low pressure plasma (Palmers, 2000). In this study a value of 94° was obtained for the non-irradiated LDPE after three measurements were carried out. The objective of this study was to compare the non-irradiated sample (baseline) with those of the irradiated samples ranging between 0 and 400kGy. As the irradiation dose increased the contact angle varied between 94° and 103°. The highest surface contact angle was observed at 150kGy and from 200 to 400 kGy the contact angle began to even out. Where the contact angle reduced, this could be attributed to the formation of hydrophilic groups such as polar species which were enhanced due to oxygen rather than the change of surface roughness (Abdul-Kader, Turos, Radwan, & Kelany, 2009; Sanchis, Blanes, Blanes, Garcia, & Balart, 2006). Hydrophilic group formation is a two-step process whereby the first step concentrates on the creation of free radicals on a polymer surface by electron beam irradiation. The second step involves interaction between free radicals in polymer chains and oxygen which results in the formation of polar groups such as carboxyl, carbonyl, hydroxyl and ester groups (Abdul-Kader, et al., 2009). Where the contact angle increased in the sample demonstrated in Fig. 3, the irradiation was causing the surface to become non-polar which in turn caused the material to repel the droplet of water (surface prefers neutral molecules). The variations throughout the graph could be attributed to the different exposure levels to oxygen during the irradiation process. Fig. 4 represents the images of the contact angles obtained for each of the non-irradiated and irradiated LDPE samples.

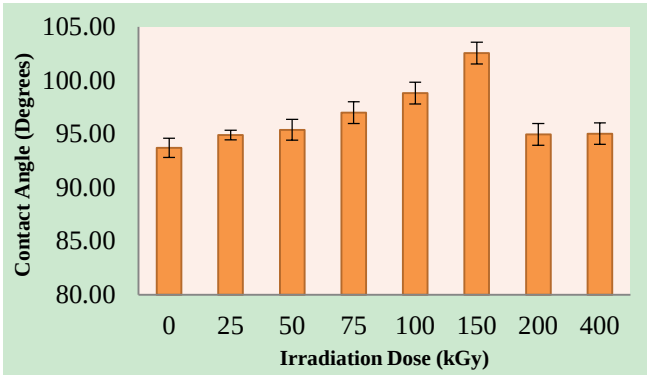

FIG. 3 VARIATION OF CONTACT ANGLE MEASUREMENTS OF LDPE AS A FUNCTION OF ELECTRON BEAM IRRADIATION DOSE

Colorimetry

Colorimetry measurements were conducted on the LDPE samples before and after irradiation with the gamma ray and electron beam processes. The exposure rate of the electron beam irradiated samples ranged between 0 and 400kGy, whilst the gamma

irradiated samples ranged between 0 and 200kGy in this experiment. The Hunter *b* value in Fig. 5 demonstrated a slight increase from -2.85 to 0.097 (400kGy) as the electron beam irradiation dose increased. This was more pronounced for the gamma irradiated samples as it increased from -2.85 to 2.01 (200kGy). Consequently, the gamma irradiated samples became more yellowish in colour. Fig. 7 displays an image of the samples after electron beam irradiation, which illustrates a slight change in colour which corresponds to the data obtained.

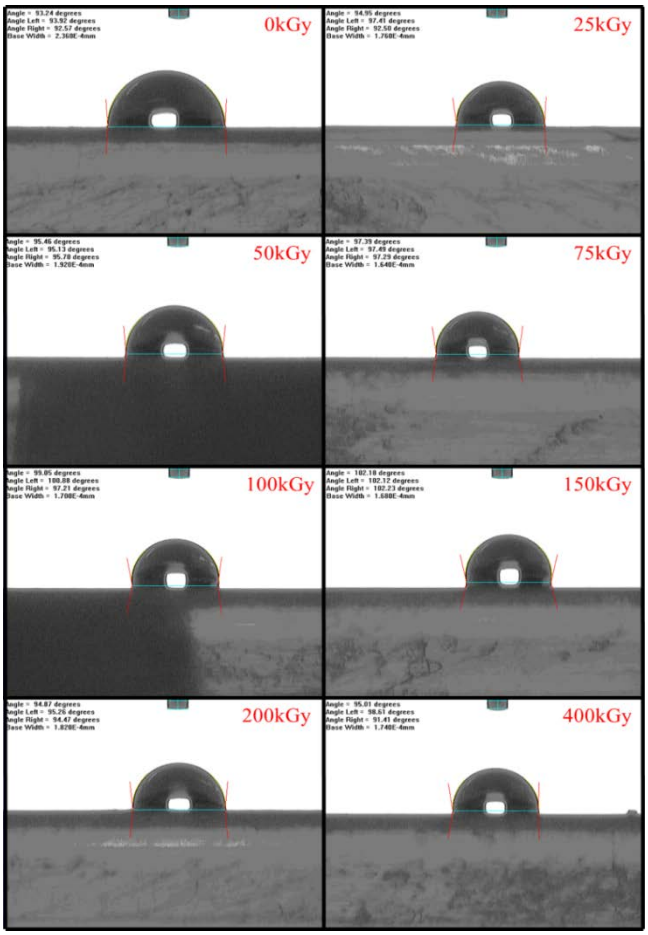

FIG. 4 CONTACT ANGLES REPRESENTING THE NON-IRRADIATED AND ELECTRON BEAM IRRADIATED LDPE SAMPLES

Fig. 6 demonstrated a slight increase for the electron beam irradiated samples with 2.94 being the overall difference as the irradiation dose increased. There was a significant increase observed for the *ΔE* value of the gamma irradiated samples with an overall difference of 14.59 as the irradiation dose increased. An explanation for such changes after the exposure of irradiation was perhaps due to the formation of conjugated double bonds and/or the entrapment of free radicals (Perera, et al., 2004). Overall, this study suggested that low density polyethylene was more sensitive to gamma ray processing in contrast to electron beam processing. This was perhaps due to the longer exposure times of irradiation during the gamma ray process.

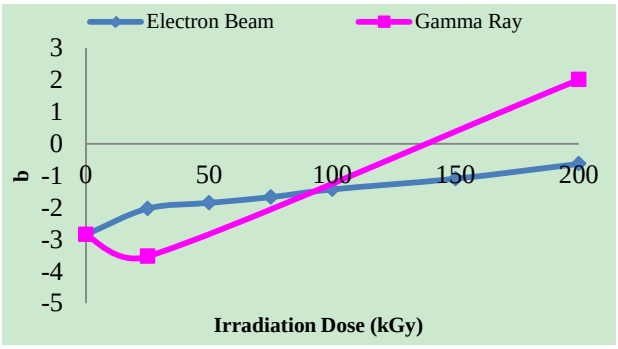

FIG. 5 HUNTER *B* VALUE FOR LDPE VS. IRRADIATION DOSE

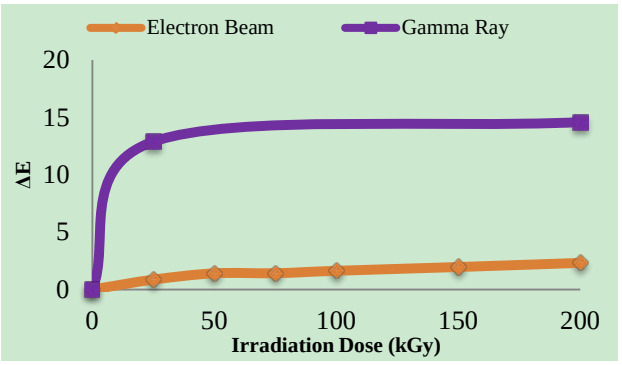

FIG. 6 HUNTER *ΔE* VALUE FOR LDPE VS. IRRADIATION DOSE

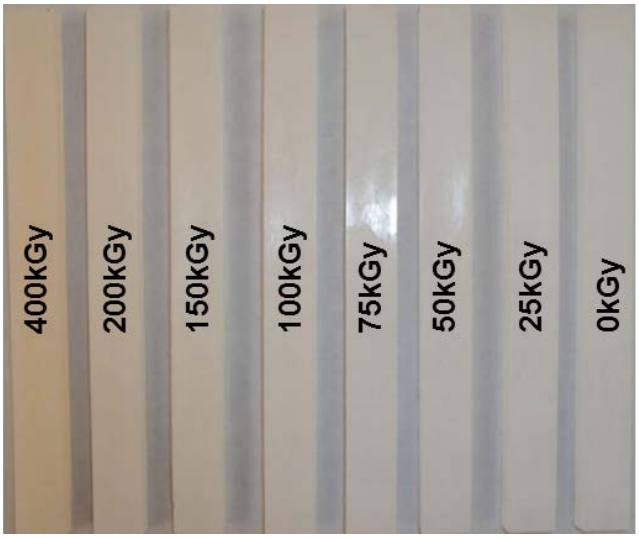

FIG. 7 COLOUR CHANGE OF LDPE BEFORE AND AFTER ELECTRON BEAM IRRADIATION

Conclusion

Despite the impossibility of getting a very accurate description of the fine details of the structure of the amorphous component, a few striking results have been obtained from the present refinements. X-ray diffraction studies implied that radiation crosslinking

occurred without significantly affecting the material crystalline structure and degree of crystallinity. The results obtained from this experiment correlated very well with the results obtained in the MDSC experiment. With regards to SEM imagery, a considerable amount of degradation transpired on the surface of the material subsequent to electron beam irradiation which could be attributed to oxidation. In addition, it was apparent from the freeze fractured samples that the fracture behaviour was influenced by electron beam irradiation. Contact angle analyses illustrated that the hydrophilic/hydrophobic characteristics of the surface functional groups varied according to different irradiation dose ranges. Irradiation resulted in the differing of surface tension values which perhaps came about from oxidation during the electron beam irradiation process. Colorimetry revealed that both the electron beam and gamma ray processes cause modifications to occur in the colour of the material. This characterisation technique aided in quantifying the discolouration for both processes and from this experiment it was evidently shown that gamma irradiation was the most detrimental method of the two.

ACKNOWLEDGMENT

The authors would like to express their sincere thanks to Enterprise Ireland for the financial support they provided towards this study. Also a special thanks to the group of operators of the gamma ray and electron beam irradiator at Synergy Health in Westport and Tullamore, Ireland, for their assistance during the irradiation of the samples in this work.

REFERENCES

Abdul-Kader, A.M., Turos, A., Radwan, R.M., Kelany, A.M. "Surface free energy of ultra-high molecular weight polyethylene modified by electron and gamma irradiation". Applied Surface Science 255 (2009): 7786-7790.

Berejka, A.J., and Cleland, M.R. "Industrial Radiation Processing With Electron Beams and X-rays". International Atomic Energy Agency, May 1, 2011. Accessed July 24, 2012. http://www.cirms.org/pdf/Industrial%20Radiation%20Processing-May%202011-Revision%206.pdf.

Bhattacharya, A. "Radiation and industrial polymers." Progress in Polymer Science 25 (2000): 371-401.

Carlos Miguez Suarez, J., and Biasotto Mano, E. "Brittle–ductile transition of gamma-irradiated recycled polyethylenes blend." Polymer Testing 19 (2000): 607-616.

Chodák, I. "High modulus polyethylene fibres: preparation, properties and modification by crosslinking." Progress in Polymer Science 23 (1998): 1409-1442.

Clough, R.L., Gillen, K.T., Malone, G.M., Wallace, J.S. "Color formation in irradiated polymers." Radiation Physics and Chemistry 48 (1996): 583-594.

Dadbin, S. "Surface modification of LDPE film by CO2 pulsed laser irradiation." European Polymer Journal 38 (2002): 2489-2495.

Dole, M. "Free Radicals in Irradiated Polyethylene." New York: Academic Press, 1972.

Garbassi, F., Morra, M., Occhielo, E. "Polymer surfaces from physics to technology." In Polymer International, edited by M.D. Purbrick, 1-2 Chichester, UK: John Wiley & Sons Ltd, 1996.

Göschel, U., and Ulrich, C. "Mechanical relaxation of medical grade UHMWPE of different crosslink density as prepared by electron beam irradiation." J. Appl. Polym. Sci. 113 (2009): 49-59.

Khonakdar, H.A., Jafari, S.H., Wagenknecht, U., Jehnichen, D. "Effect of electron-irradiation on cross-link density and crystalline structure of low- and high-density polyethylene." Radiation Physics and Chemistry 75 (2006): 78-86.

Kurtz, S.M. "The UHMWPE Handbook." Amsterdam: Elsevier Academic Press, 2004.

Lazar, M., Rado, R., Rychlý, J. "Crosslinking of polyolefins." Adv Polym Sci 95 (1990): 149-197.

Lustiger, A., and Corneliussen, R.D. "The role of crazes in the crack growth of polyethylene." Journal of Materials Science 22 (1987): 2470-2476.

Murray, K.A., Kennedy, J.E., McEvoy, B., Vrain, O., Ryan, D., Cowman, R., Higginbotham, C.L. "Effects of gamma ray and electron beam irradiation on the mechanical, thermal, structural and physicochemical properties of poly (ether-block-amide) thermoplastic elastomers." Journal of the Mechanical Behavior of Biomedical Materials 17 (2013a): 252-268.

Murray, K.A., Kennedy, J.E., McEvoy, B., Vrain, O., Ryan, D.,

Cowman, R., Higginbotham, C.L. "The effects of high energy electron beam irradiation in air on accelerated aging and on the structure property relationships of low density polyethylene." Nuclear Instruments and Methods in Physics Research Section B: Beam Interactions with Materials and Atoms 297 (2013b): 64-74.

Murray, K.A., Kennedy, J.E., McEvoy, B., Vrain, O., Ryan, D., Higginbotham, C.L. "The effects of high energy electron beam irradiation on the thermal and structural properties of low density polyethylene." Radiation Physics and Chemistry 81 (2012): 962-966.

Niemantsverdriet, J.W. "Spectroscopy in catalysis an introduction." Weinheim: Wiley-VCH-Verl, 2007.

Palmers, J. "Surface modification using low-pressure plasma technology," Medical Device & Diagnostic Industry Magazine, 2000.

Perera, R., Albano, C., González, J., Silva, P., Ichazo, M. "The effect of gamma radiation on the properties of polypropylene blends with styrene-butadiene-styrene copolymers." Polymer Degradation and Stability 85 (2004): 741-750.

Salovey, R. "Irradiation of crystalline polyethylene." Journal of Polymer Science 61 (1962): 463-473.

Sanchis, M.R., Blanes, V., Blanes, M., Garcia, D., Balart, R. "Surface modification of low density polyethylene (LDPE) film by low pressure O2 plasma treatment." European Polymer Journal 42 (2006): 1558-1568.

Sharif, J., Aziz, S.H.S.A., Hashim, K. "Radiation effects on LDPE/EVA blends." Radiation Physics and Chemistry 58 (2000): 191-195.

Singh, L., and Singh, R. "Swift heavy ion induced modifications in polypropylene." Nuclear Instruments and Methods in Physics Research Section B: Beam Interactions with Materials and Atoms 225 (2004): 478-482.

Singh, R., Samra, K.S., Kumar, R., Singh, L. "Proton (3 MeV) and copper (120 MeV) ion irradiation effects in low-density polyethylene (LDPE)." Radiation Physics and Chemistry 77 (2008): 53-57.

Smedberg, A., Hjertberg, T., Gustafsson, B. "Crosslinking reactions in an unsaturated low density polyethylene." Polymer 38 (1997): 4127-4138.

Suarez, J.C.M., da Costa Monteiro, E.E., Mano, E.B. "Study of the effect of gamma irradiation on polyolefins--low-density polyethylene." Polymer Degradation and Stability 75 (2002): 143-151.

Suarez, J.C.M., and Mano, E.B. "Characterization of degradation on gamma-irradiated recycled polyethylene blends by scanning electron microscopy." Polymer Degradation and Stability 72 (2001): 217-221.

Suryanarayana, C., and Norton, M.G. "X-ray diffraction, a practical approach." New York: Plenum Press, 1998.

Viksne, A., Zicans, J., Kalkis, V., Bledzki, A.K. "Heat-shrinkable films based on polyolefin waste." Die Angewandte Makromolekulare Chemie 249 (1997): 151-162.

Yan, R.J., Luo, Y., Jiang, B. "The effect of radiation-induced cross-linking on the relaxation of taut tie molecules during annealing of drawn LDPE." Journal of Applied Polymer Science 47 (1993): 789-796.

Modeling Rheological Properties Of Oil Well Cement Slurries Using Multiple Regression Analysis And Artificial Neural Networks

Anjuman Shahriar [*1], Moncef Nehdi [2]

Department of Civil and Environmental Engineering, The University of Western Ontario
London, ON, N6A 5B9, Canada
[*1]anjuman.shahriar@gmail.com; [2]mnehdi@uwo.ca.

Abstract

Artificial neural networks (ANN) and multiple regression analysis (MRA) were used to predict the rheological properties of oil well cement slurries. The slurries were prepared using class G oil well cement with a water-cement mass ratio (w/c) of 0.44, and incorporating a new generation polycarboxylate-based high-range water reducing admixture (PCH), polycarboxlate-based mid-range water reducing admixture (PCM), and lignosulphonate-based mid-range water reducing admixture (LSM). The rheological properties were investigated at different temperatures in the range of 23 to 60ºC using an advanced shear-stress/shear-strain controlled rheometer. Experimental data thus obtained were used to develop predictive models based on back-propagation artificial neural networks and multiple regression analysis. It was found that both ANN and MRA depicted good agreement with the experimental data, with ANN achieving more accurate predictions. The developed models could effectively predict the rheological properties of new slurries designed within the range of input parameters of the experimental database with an absolute error of 3.43, 3.17, and 2.82%, in the case of ANN and 4.83, 6.32, and 5.05%, in the case of MRA, for slurries incorporating PCH, PCM, and LSM, respectively. The flow curves developed using ANN and MRA allowed predicting the Bingham parameters (yield stress and plastic viscosity) of the oil well slurries with adequate accuracy.

Keywords

Cement slurry; Oil well; Yield stress; Plastic viscosity; Artificial neural network; Multiple regression analysis.

1. Introduction

The recent oil spill in the Gulf of Mexico and the associated environmental and economic impact has put renewed emphasis on the importance of oil well cementing operations. The rheological properties of oil well cement (OWC) slurries are important in assuring that such slurries can be mixed at the surface and pumped into the well with minimum pressure drop, thereby achieving effective well cementing operation. The rheological properties of OWC slurries depend on various factors including the water-cement ratio (w/c), size and shape of cement grains, chemical composition of the cement and relative distribution of its components at the surface of grains, presence and type of additives, compatibility between cement and chemical admixtures, mixing and testing procedures, time and temperature, etc. The interactions among the above mentioned factors play a vital role in altering the rheological properties of OWC slurries. Moreover, a wide range of bottom-hole pressure and temperature makes the characterization of the rheology of OWC slurries more challenging than that of normal cement paste. Therefore, a clear understanding of this complex behavior is important in order to successfully predict the rheological properties of OWC slurries.

Much work has been conducted over the last few decades to investigate the rheological behaviour of cementitious systems such as cement paste, mortar, grout, slurry and concrete. A number of shear stress-strain rate relationships have been developed for cement slurries. However, there exists no model that explains the interactions among the materials used for preparing such slurries and test conditions such as temperature, shear rate, etc. The power-law, Bingham, and Herschel-Bulkley models are the most commonly used in the well cementing industry [Guillot 2006]. Such models are comprised of empirical expressions derived from the analysis of limited experimental data and/or based on simplifying assumptions [El-Chabib and Nehdi 2005]. Moreover, they do not have true predictive capability outside the experimental domain and/or when different materials are used [El-Chabib et al. 2003], and do not explain the interactions among test parameters.

ANN is a powerful computational tool that allows overcoming the difficulty of assessing the complex and highly nonlinear relationships among model parameters through self-organization, pattern recognition, and functional approximation. ANN simulates the structure and internal functions of the biological brain. Unlike conventional models, ANN does not assume a model structure between input and output variables. It rather generates the model based on the database provided for training the network. An ANN solves problems by creating parallel networks and the training/learning of those networks, rather than by a specific programming scheme based on well-defined rules or assumptions [Bruni et al. 2006].

On the other hand, multiple regression analysis (MRA) is a statistical method to learn about the analytical relationship between several independent or predictor variables (input variables) and a dependent or criterion variable (output variable) [Statsoft 2010]. The relations may be linear or nonlinear, and independent variables may be quantitative or qualitative. MRA explains the effects of a single input variable or multiple variables on the output variable with or without considering the effects of other variables [Cohen et al., 2003].

Temperature has been found to have drastic effects on the rheological behavior of cement slurries. Its effect also depends on the type of cement and admixtures used. Thus, it was argued that it would be difficult to find a general model that can represent the temperature dependency of cement slurry rheology [Guillot 2006]. Ravi and Sutton [1990] developed a correlation to calculate the equilibrium temperature for plastic viscosity and yield stress of Class H cement slurries using a high-pressure, high-temperature rheometer. It was found that both plastic viscosity and yield stress increased with the increase in temperature. However, plastic viscosity reached a constant value beyond the equilibrium temperature, whereas there was no evidence for yield stress to attain a constant value beyond a certain temperature. Using the Bingham plastic model, Ravi and Sutton [1990] developed equations to represent the variation of rheological parameters with temperature where the yield stress and plastic viscosity values were measured at 80°F (27°C) and limited to a maximum temperature, Tmax. Their equations below were developed using cement systems containing specific additives, and are thus dependent on the slurry composition.

$$\mu_p(T) = a + (b \times T) + (0.00325 \times T^2) \qquad (1)$$

Where, is in mPa.s and T is in °F; and at 80°F; and at 80°F.

Currently, there is need to create a reliable method for predicting the rheological performance of OWC slurries and relating its composition (admixture type, dosage, etc.) and test conditions (e.g. shear rate, temperature) to the expected rheological properties. In this framework, ANN and MRA have been used in the present study to develop models to predict the shear stress of OWC slurries at a given shear rate, as a function of the temperature and admixture dosage. The ability of the models thus developed to evaluate the sensitivity of rheological properties to the variation of shear rate, admixture dosage, and test temperature was investigated. Hence, a shear stress-shear rate curve for OWC slurries can be predicted at different temperatures prior to fitting the data to conventional rheological models. Consequently, the rheological properties of OWC slurries can be predicted as a function of mixture composition and test conditions for the first time.

2. Experimental Program

2.1 Materials

OWC slurries used in this study were prepared using a high sulphate-resistant API Class G OWC with a specific gravity of 3.14. Deionized distilled water was used for the mixing, and its temperature was maintained at 23±1°C using an isothermal container. Three different chemical admixtures including a new generation polycarboxylate-based high-range water reducing admixture (PCH), polycarboxylate-based mid-range water reducing admixture (PCM) and mid-range lignosulphonate based water reducing admixture (LSM) were used to prepare the OWC slurries with a w/c = 0.44. Their dosages are presented in Table 1.

2.2. Apparatus

The OWC slurries were prepared using a variable speed high-shear blender type mixer with bottom drive blades as per the ANSI/API Recommended Practice 10B-2 [2005]. A high accuracy advanced rheometer (TA instruments AR 2000) (Fig. 1(a)) was used to measure the rheological properties of the slurries. The rheometer is capable of continuous shear rate sweep and stress sweep. The coaxial

concentric cylinder geometry was considered suitable for this study because of the typically low viscosity of OWC slurries.

TABLE 1 CHEMICAL ADMIXTURES USED FOR PREPARING OIL WELL CEMENT SLURRIES

Type of admixture	Abbreviation	Dosages % BWOC*
New generation polycarboxylate-based high-range water reducing admixture	PCH	0.25, 0.50, 0.75, and 1.00
Polycarboxylate-based mid-range water reducing admixture	PCM	0.25, 0.50, 0.75, and 1.00
Mid-range lignosulphonate based water reducing admixture	LSM	0.5, 1.0, 1.5 and 2.0

* BWOC: by weight of cement

The geometry consists of a cylinder with a conical end that rotates inside a cylinder with a central fixed hollow as shown in Fig. 1(b). This smooth inner solid cylinder rotates inside a fixed hollow cylinder of 15 mm in diameter. The gap between the head of the conical end and the bottom of the hollow cylinder was set to 0.5 mm for all experiments. It is required to use such a narrow gap in order to main a constant shear rate across the gap, which is important, especially in case of static flow studies to minimize the error caused by wall slip in rheological measurements [Saak et al. 2001]. The rheometer maintains an auto gap in order to compensate for the expansion of the stainless steel of the coaxial concentric cylinders under a wide range of temperatures, thus keeping the gap constant during experiments. The calibration of the rheometer was performed using a certified standard Newtonian oil with a known viscosity of 1.0 Pa.s and yield stress = 0 Pa at 20°C. The measured yield stress was 0 Pa and viscosity was 1.009 Pa.s with an error of 0.9%, which is less than the tolerated error of 4% specified by the manufacturer. The rheometer is equipped with a rheological data analysis software, which can fit the shear stress-strain rate data to several rheological models. The Bingham model was used throughout this study to calculate the rheological properties of cement slurries, i.e. yield stress and plastic viscosity.

(A)

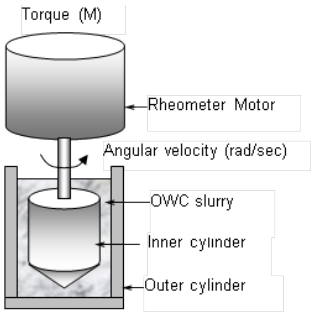

(B)

FIG. 1 ILLUSTRATION OF, (A) ADVANCED RHEOMETER WITH COAXIAL CYLINDER GEOMETRY, AND (B) COAXIAL CONCENTRIC CYLINDER WITH CYLINDRICAL CONICAL END GEOMETRY.

3. Experimental Procedure

A high-shear blender type mixer with bottom driven blades was used to prepare the slurry according to the following procedure. First, the weighed amount of cement and solid admixture (if any) were manually dry mixed in a bowl using a spatula for about 30 sec. The mixing water was subsequently poured into the blender. Then the required quantity of liquid admixture was added into the mixing water using a needle. The mixing resumed at slow speed for 15 sec so that chemical admixtures could be thoroughly dispersed in water. The cement was added to the liquids (chemical admixture and water) over a period of 15 sec. Manual mixing was conducted for another 15 sec and a rubber spatula was used to recover any material sticking to the wall of the mixing container to ensure homogeneity. Finally, mixing resumed for another 35 sec at high speed. This mixing procedure was strictly followed for all cement slurries and all mixing was conducted at a controlled ambient room temperature of 23±1°C. The prepared slurry was then placed into the bowl of a mixer for preconditioning (at

150 rpm) over 20 minutes at the specific test temperature (23°C, 45°C, or 60°C). The total time between the beginning of mixing and the start of the rheological tests was kept constant to avoid the effects of exogenous variables on the results. The rheometer set-up was also maintained constant for all tested slurries. The concentric cylinder test geometry was maintained at the test temperature so as to avoid sudden thermal shock of the slurry.

After mixing and preconditioninfg, the cement slurry sample was placed in the coaxial cylinder of the rheometer. The temperature was adjusted to the required level and the sample was then subjected to a stepped ramp or steady state flow where rheological measurements were taken at 20 different shear rates starting from 5.11 s^{-1} up to 511 s^{-1} after a continuous rotation of 10 sec at each level. Subsequently, the data were measured at a descending shear rate from 511 s^{-1} to 5.11 s^{-1} to obtain the down flow curve. A schematic representation of the viscometric testing scheme is illustrated in Fig. 2.

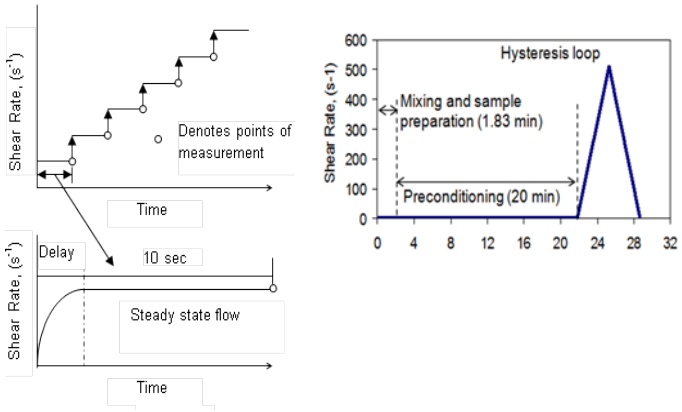

(A) (B)

FIG. 2 (A) SCHEMATIC REPRESENTATION OF STEPPED RAMP, AND (B) RHEOMETER TEST SEQUENCE (SHEAR RATE HISTORY USED IN RHEOLOGICAL TESTS).

4. Experimental Results

Typical shear stress-shear rate down curves of the hysteresis loop for OWC slurries prepared using a new generation polycarboxylate-based high-range water reducing admixture (PCH) at 60°C are presented in Fig. 3. The down-curve better fits the Bingham plastic model than the up-curve [Ferguson and Kemblowski 1991, Al-Martini and Nehdi 2009], therefore the shear rate–shear stress down curve was considered in calculating the rheological properties (yield stress and plastic viscosity) using the Bingham plastic model (equation 2). The rheological parameters thus calculated are highly dependent on the temperature and admixture dosage as can be observed in Figs. 4 and 5.

$$\tau = \tau_0 + \mu_P \bar{\gamma} \quad (2)$$

Where, τ , τ_0 , μ_P , and $\bar{\gamma}$ represent the shear stress, yield stress, plastic viscosity, and shear rate, respectively.

In this study, two different approaches: MRA and ANN have been used to predict the shear stress as a function of test variables (temperature, admixture dosage and shear rate). The predicted flow curve allows in turn predicting the rheological properties of OWC slurries. Hence model predictions and corresponding experimental data can be compared.

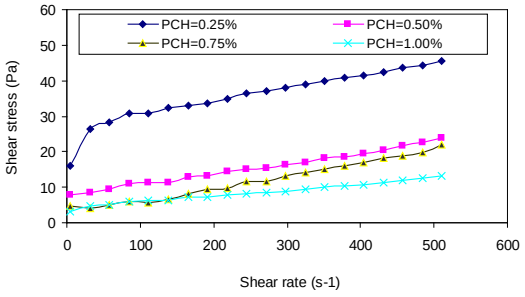

FIG. 3 SHEAR STRESS-SHEAR RATE DOWN CURVE FOR OWC SLURRIES PREPARED USING DIFFERENT DOSAGE OF PCH AT 60°C.

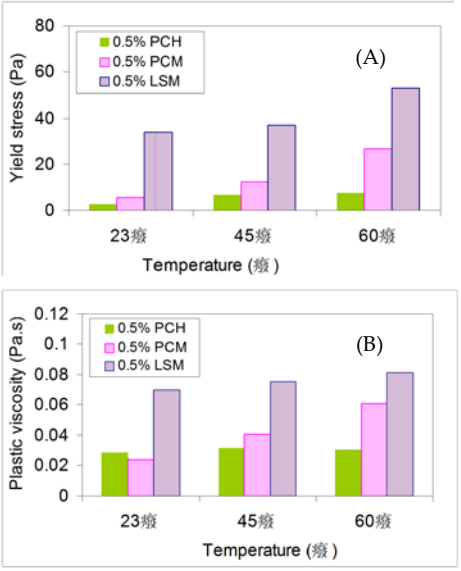

FIG. 4 EFFECT OF TEMPERATURE ON (A) YIELD STRESS, AND (B) LASTIC VISCOSITY OF OWC SLURRY PREPARED USING DIFFERENT ADMIXTURES (0.5% BWOC).

5. Artificial Neural Networks Approach

An ANN is capable of learning the mapping between a set of input data and its corresponding output.

Through training, it becomes capable of predicting output when presented with a new set of data within the practical range of the input used in the training process. The feed-forward back-propagation learning algorithm is the most commonly used in engineering applications, especially in modelling the behaviour of cement based materials. A neural network consists of an input layer, one or more hidden layers, and an output layer of several interconnected linear or nonlinear processing units (neurons). Each processing unit receives multiple inputs from the neurons in the previous layer through the weighted connection, and after performing appropriate computation, transfers its output to other processing units or as a network output using an assigned transfer (activation) function as shown in Fig. 6. In this study, a feed-forward back-propagation neural network was developed to predict the rheological parameters of OWC slurries. The topography and training parameters obtained through trial and error for the ANN model thus developed are presented in Fig. 7 and Table 2, respectively. The model parameters were selected based on the lowest training and testing error. It should be noted that different network architectures can provide satisfactory performance for the same application.

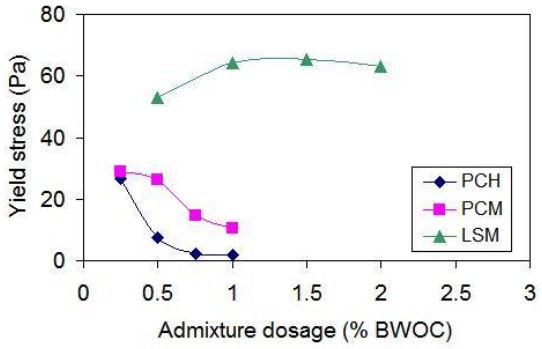

(A)

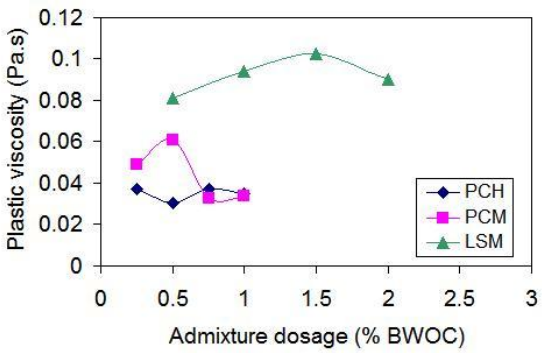

(B)

FIG. 5 EFFECT OF ADMIXTURE DOSAGE ON (A) YIELD STRESS, AND (B) PLASTIC VISCOSITY OF OWC SLURRY PREPARED USING DIFFERENT ADMIXTURES AT 60°C.

Although ANN have been successfully used in predicting complex nonlinear relationships and in modeling various aspects in cement and concrete research, their efficiency depends on the quality of the database used for training the network architecture, and network training and testing [El-Chabib et al. 2003]. In order to train the model, 570 data points generated in the experimental study described above were used (190 data points for each of the three admixtures tested: PCH, PCM and LSM). Another 150 new data points (50 data points for each of the three admixtures tested: PCH, PCM and LSM) not used in the training, and hence, unfamiliar to the model, but within the range of training data, were used to test the performance of the network. It should be noted that each flow curve consists of 20 data points at equal shear rate intervals starting from 5.11 s^{-1} to 511 s^{-1}.

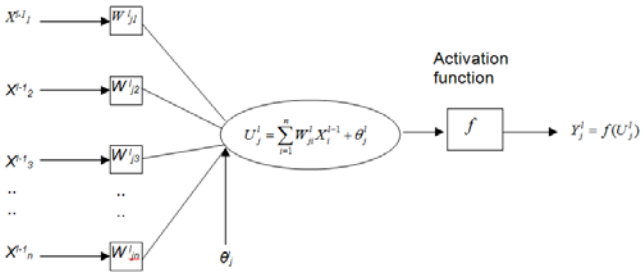

FIG. 6 SIMPLIFIED MODEL OF ARTIFICIAL NEURAL NETWORK

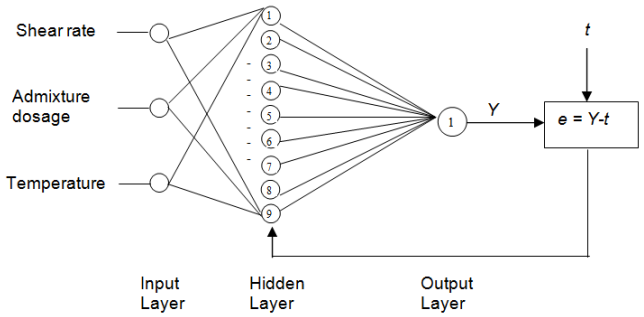

FIG. 7 ARCHITECTURE OF DEVELOPED ANN MODEL.

TABLE 2 TOPOGRAPHY AND TRAINING PARAMETERS FOR THE DEVELOPED ANN MODEL

Number of input nodes	3
Number of output nodes	1
Number of hidden layers	1
Number of nodes in hidden layers	9
Activation function input-hidden layers	Log-sigmoid
Activation function hidden-output layers	Linear
Distribution of weights	Gaussian
Momentum coefficient	0.03
Learning rate	0.05
Convergence	$5E^{-8}$

Specialized commercial computer software [Demuth et al. 2008] was used to train the feed-forward back-propagation neural network in order to predict the

rheological properties of OWC slurries. Supervised training was implemented in this study by providing the network with sets of data (inputs/targets) and the network was instructed what to learn. Parameters such as the learning rate and convergence tolerance used for the ANN are presented in Table 2. A training pattern consists of an input vector of 3 elements including the admixture dosage, temperature and shear rate, and a corresponding output vector consisting of shear stress. The unipolar log-sigmoid (logsig) function and linear function were assigned as the transfer function for the processing units in the input-hidden layers and the hidden-output layers, respectively. Full connection between the processing units in adjacent layers was adopted, whereas no connection was permitted between neurons in the same layer.

After completion of each learning process, the average sum-squared of all errors was calculated and back-propagated through the Levenberg-Marquardt algorithm [Demuth et al. 2008] to adjust the weights or connection strengths between the processing units. This iterative process can continue until the difference between the network prediction and the provided targets is virtually zero. Such over-training, known as over-fitting will not provide acceptable prediction when presented to new mixtures excluded from the training data [El-Chabib et al. 2003]. In order to avoid over-fitting, the iteration was forced to stop early by setting the convergence tolerance or the average sum-squared errors (ASSE) between the training sets and target sets = $5E^{-5}$.

6. Multiple Regression Analysis

In the MRA-based approach, the dependent variables yield stress and plastic viscosity were correlated to the independent variables; i.e. shear rate, admixture dosage, and test temperature using first (linear) and then (polynomial) order regression models. It was found that no substantial improvement was achieved by the polynomial regression. Therefore, the linear regression-based approach was used to observe the effect of temperature, admixture dosages and shear rate on shear stress. As a consequence, the shear stress values versus shear rate, admixture dosage and test temperature, were predicted using the following relationship:

$$\tau = a + b\bar{\gamma} + cD_A + dT + e\bar{\gamma}D_A + f\bar{\gamma}T + gD_AT + h\bar{\gamma}D_AT \quad (3)$$

where, *a*, *b*, *c*, *d*, *e*, *f*, *g*, and *h* are regression coefficients, and τ, $\bar{\gamma}$, D_A and T are the shear stress, shear rate, dosage of admixture and temperature, respectively.

In order to perform the regression analysis, a total of 240 data points from down curves of the hysteresis loops were used for each of the three admixtures tested (PCH, PCM and LSM). Each data point consists of 3 input variables including shear rate, dosage of admixture and temperature, and one output parameter: shear stress. The least square approach was followed to estimate the coefficients of the model parameters. The interaction between the considered three input parameters and the output parameter were also accounted for during the regression analyses and expressed in terms of t and probability (Prob.>|t|) values. The probability value indicates the probability that the result obtained in a statistical test is due to chance rather than to a true relationship between the parameters [Genentech 2010, Montgomery 2009]. The effects of the input parameters on the output parameters are considered highly significant when t values are high and probability values are low. The parameter is often considered nonzero and significantly influences the response of the model when the probability values are less than 5% [Sonebi 2001, Health and Income Equity 2010].

7. Model Performance

The developed models using the ANN and MRA techniques predicted the shear stress of the OWC slurries and the acceptability/rejection of the model was evaluated using the average absolute error (AAE) given by equation 4 and the correlation coefficient (R2).

$$AAE = \frac{1}{n}\sum_{i=1}^{n}\frac{\left|\tau_{measured} - \tau_{predicted}\right|}{\tau_{measured}} \quad (4)$$

where $\tau_{measured}$ and $\tau_{predicted}$ are the experimentally measured shear stress value of OWC slurries and the corresponding data predicted by the model, respectively, and n is the total number of data points.

7.1. Validation of ANN and MRA-Based Models

The artificial neural network model shown in Fig. 7 was trained using 190 training (input/target) pairs for each of the admixtures investigated, and tested using 50 pairs of new data points unfamiliar to the network and not used in the training process.

Figures 8, 9 and 10 illustrate the performance of the ANN in predicting the shear stress of OWC slurries incorporating PCN, PCM, and LSM, respectively. After successful completion of the training process,

the network performance in predicting the shear stress of OWC slurries incorporating PCH was investigated and the results are presented in Fig. 8(a). It can be observed that all data points are located on or in the vicinity of the equity line with an AAE of 3.43%. For cement slurries incorporating PCM, the relationship between measured and predicted shear stress is presented in Fig. 9(a). The model was successfully trained to predict the shear flow with an AAE of 3.17%. Similarly, Fig. 10(a) represents the performance of the ANN model in predicting the shear stress of cement slurries incorporating LSM. It can be observed that the model was able to predict the shear stress of the cement slurries satisfactorily since the measured and corresponding predicted data points are located along the equity line with an AAE of 2.82%.

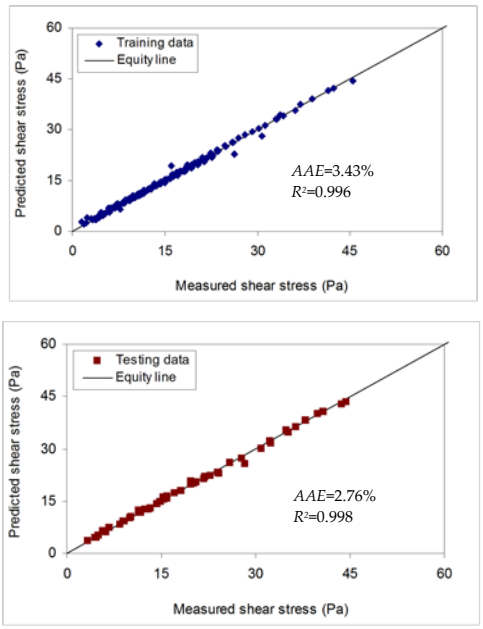

FIG. 8 MEASURED VERSUS ANN-MODEL PREDICTED SHEAR STRESS FOR OWC SLURRIES INCORPORATING PCH.

The acceptance/rejection of the ANN model depends primarily on its performance in predicting the shear stress of new sets of unfamiliar data within the range of input variables of training patterns. In order to validate the developed model, the network was presented with 50 new sets of data which were not used in training the network. In this case, only input vectors of shear rate, dosage of admixture and temperature were presented to the network and no information or knowledge about the corresponding shear stress was provided. The response of the neural network is presented in Figs. 8(b), 9(b) and 10(b) for OWC mixtures made with PCH, PCM and LSM, respectively. The model predictions are accurate since the testing points are located slightly over or under the equity line but within the cluster of training data with an AAE of 2.76, 2.77 and 2.81% for slurries with PCH, PCM and LSM, respectively.

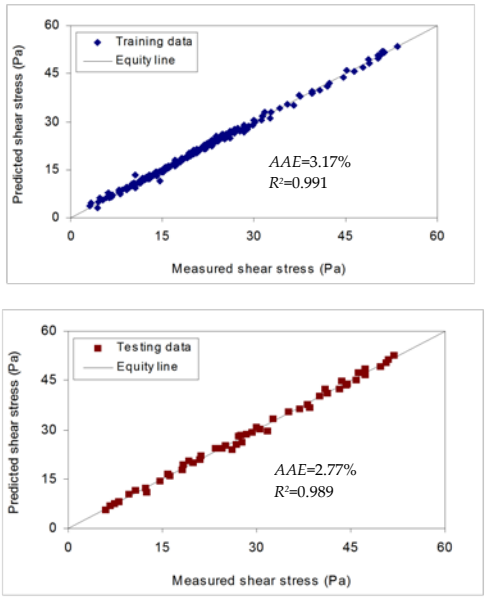

FIG. 9 MEASURED VERSUS ANN-MODEL PREDICTED SHEAR STRESS FOR OWC SLURRIES INCORPORATING PCM.

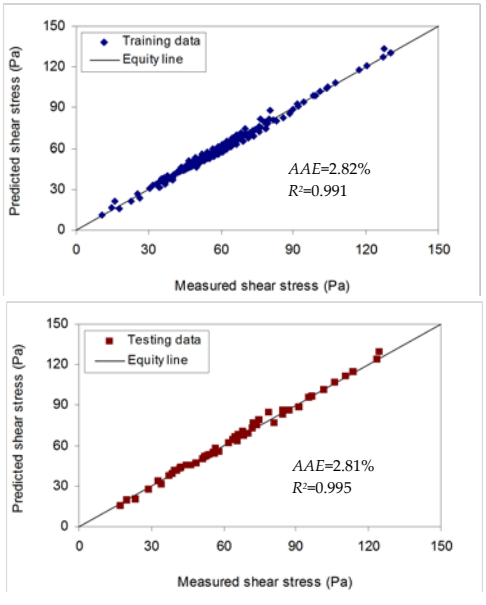

FIG. 10 MEASURED VERSUS ANN-MODEL PREDICTED SHEAR STRESS FOR OWC SLURRIES INCORPORATING LSM.

Figure 11 (a, b, c) represents the performance of models using the MRA technique in predicting the shear stress of OWC slurries incorporating PCH, PCM and LSM, respectively. All data points are

located on or in the vicinity of the equity line with an AAE of 4.83, 6.32 and 5.05% for slurries with PCH, PCM and LSM, respectively.

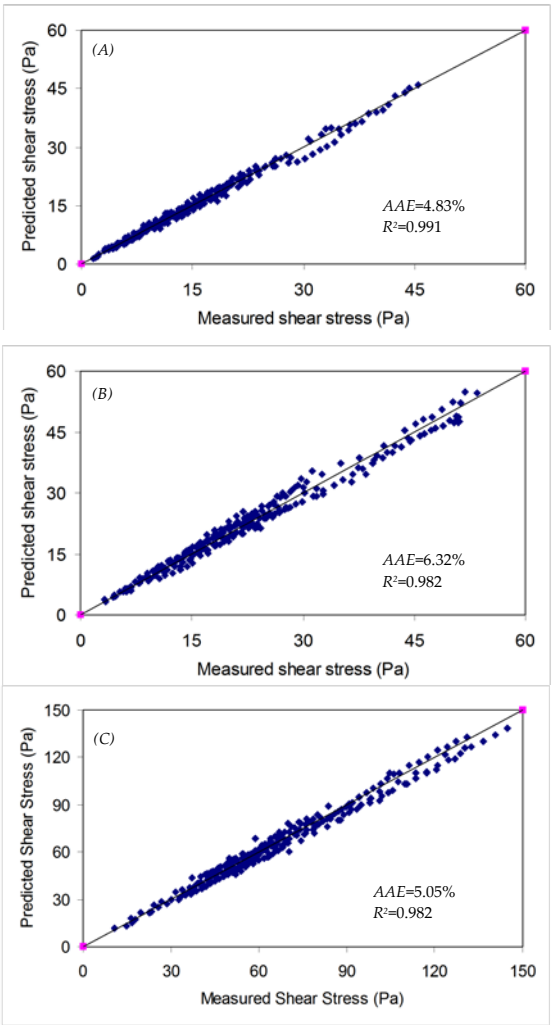

FIGURE 11 MEASURED VERSUS MRA–MODEL PREDICTED SHEAR STRESS FOR OWC SLURRIES INCORPORATING (A) PCH, (B) PCM, AND (C) LSM.

Table 3 reveals the relative importance of various parameters as well as their interactions in predicting the shear stress of OWC slurries prepared with PCH, PCM and LSM. It can be observed that the probabilities of the derived coefficients of all the parameters for PCH and PCM are limited to 3.9%. This implies that there is less than 3.9% chance, or 96.1% confidence limit, that the contribution of a given parameter to the tested response exceeds the value of the specified coefficient. In case of LSM, the probabilities of the derived coefficients of all the parameters are limited to 4.9%. Negative coefficients suggest that an increase of the given parameter results in a reduction of the measured response. Moreover, the value/coefficient of the parameter represents the importance of the given parameter on the response value. The higher the coefficient of the parameter, the greater is its influence. For example, an increase in temperature increases the shear stress for all the admixtures tested, and an increase in the dosage of the admixture reduces the shear stress in the case of PCH and PCM, but increases the response value in the case of LSM, which is in good agreement with the experimental results. Moreover, the admixture dosage was found to have more influence on the model response than that of the other parameters. The presence of interactions with coupled terms specifies that the influence of the parameter on a particular response is quadratic [Sonebi 2001].

The derived statistical models using the multiple regression analysis approach for shear stress of OWC slurries incorporating PCH, PCM and LSM have been selected based on the lowest average absolute error (AAE) and the highest correlation coefficient/determination coefficient (R2); they are given in Equations (5), (6) and (7), respectively.

$$\tau = 5.0 - 0.013\bar{\gamma} - 5.075D_A + 0.279T + 0.076\bar{\gamma}D_A + 0.001\bar{\gamma}\mathrm{T} - 0.256D_AT - 0.002\bar{\gamma}D_AT \quad (5)$$

$$\tau = 5.0 - 0.022\bar{\gamma} - 8.849D_A + 0.429T + 0.085\bar{\gamma}D_A + 0.002\bar{\gamma}\mathrm{T} - 0.220D_AT - 0.002\bar{\gamma}D_AT \quad (6)$$

$$\tau = 0.122\bar{\gamma} + 4.909D_A + 0.869T - 0.068\bar{\gamma}D_A - 0.072D_AT + 0.002\bar{\gamma}D_AT \quad (7)$$

The accuracy of the ANN- and MRA-based models thus developed was further evaluated by comparing the ratio of the measured-to-predicted values of the shear stress of OWC slurries. The maximum, minimum and average of the shear stress values, standard deviation (*SD*), and coefficient of variation (*COV*) and the average absolute error (*AAE*) for all the data are presented in Tables 4 and 5. The results reveal that both the ANN and MRA have successfully learned to map between input parameters (shear rate, dosage of respective admixture, temperature) and corresponding output (shear stress). The proposed models satisfactorily predicted the shear stress with acceptable error. However, the *AAE* of the models developed using the ANN approach was found to be lower than that of MRA-based models. The better performance of the ANN-based model was also supported by the higher correlation coefficient (R^2) than that provided by the MRA-based models.

7.2. Performance of ANN and MRA in Predicting Rheological Properties of OWC Slurries

Based on the satisfactory performance of the developed ANN and MRA models in predicting the shear stress of OWC slurries, the down flow curve for a particular mixture was predicted by changing the shear rate and keeping the admixture dosage and temperature unchanged. Subsequently, stress-shear rate curve corresponding to a zero shear rate, and the plastic viscosity was the slope of the curve. One slurry mixture for each of the admixtures was randomly selected from the testing data and used to develop the down flow curve at different temperatures (23°C, 45°C, and 60°C). These OWC mixtures were made with 0.5% of each admixture.

TABLE 3 MODEL PARAMETERS

	PCH (R^2 = 0.991)			PCM (R^2 = 0.982)			LSM (R^2 = 0.982)		
	Coeff.	*t*	*Prob.>|t|*	*Coeff.*	*t*	*Prob.>|t|*	*Coeff.*	*t*	*Prob.>|t|*
Intercept	5.000	-	-	5.000	-	-	0.000	-	-
$\overline{\gamma}$	-0.013	-2.076	0.039	-0.022	-3.439	0.001	0.122	7.514	< 0.0001
D_A	-5.075	-2.329	0.021	-8.849	-4.026	< 0.0001	4.909	1.723	0.086
T	0.279	10.323	< 0.0001	0.429	15.696	< 0.0001	0.869	12.275	< 0.0001
$\overline{\gamma} xD_A$	0.076	6.860	< 0.0001	0.085	7.633	< 0.0001	-0.068	-4.748	< 0.0001
$\overline{\gamma} xT$	0.001	7.765	< 0.0001	0.002	10.683	< 0.0001	0.000	-1.178	0.240
$D_A xT$	-0.265	-4.407	< 0.0001	-0.220	-3.619	0.000	-0.072	-0.919	0.359
$\overline{\gamma} xD_A xT$	-0.002	-7.329	< 0.0001	-0.002	-8.514	< 0.0001	0.002	5.030	< 0.0001

TABLE 4 PERFORMANCE OF ANN-BASED MODEL IN PREDICTING THE SHEAR STRESS OF CEMENT SLURRIES PREPARED WITH DIFFERENT CHEMICAL ADMIXTURES

Type of admixture	*AAE (%)*		$\tau_{measured}/\tau_{predicted}$					
			Average		*SD*[1]		*COV*[2] (%)	
	Training	Testing	Training	Testing	Training	Testing	Training	Testing
PCH	3.43	2.76	0.984	0.988	0.058	0.040	5.88	4.09
PCM	3.17	2.77	0.998	1.001	0.062	0.040	6.18	4.01
LSM	2.82	2.81	1.000	1.000	0.042	0.041	4.23	4.11

[1]SD: standard deviation, [2] $COV = SD / Average * 100$

TABLE 5 PERFORMANCE OF MRA-BASED MODEL IN PREDICTING THE SHEAR STRESS OF CEMENT SLURRIES PREPARED WITH DIFFERENT CHEMICAL ADMIXTURES

Type of admixture	*AAE (%)*	$\tau_{measured}/\tau_{predicted}$				
		Maximum	*Minimum*	*Average*	*SD*[1]	*COV*[2] (%)
PCH	4.83	1.165	0.805	1.006	0.062	6.128
PCM	6.32	1.203	0.864	0.999	0.073	7.348
LSM	5.05	1.167	0.854	1.018	0.059	5.804

[1]*SD*: standard deviation, [2] $COV = SD / Average * 100$

Figure 12 (a, b) represents the predicted yield stress and plastic viscosity values, respectively for OWC slurries incorporating 0.5% of PCH, PCM, and LSM at different temperatures, along with the corresponding experimentally measured values. Both the yield stress and plastic viscosity values predicted by the ANN- and MRA-based models followed a similar trend to that of the experimental data. In addition to test temperatures (23°C, 45°C and 60°C), rheological parameters were also determined at 35°C and 52°C in

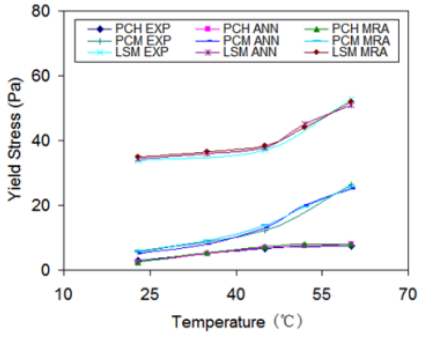

(A)

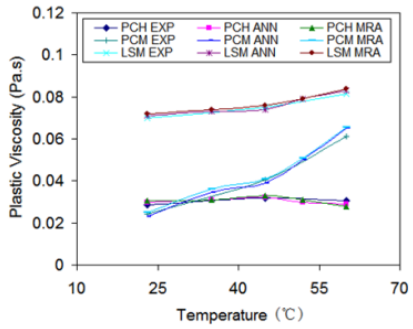

(B)

FIG. 12 VARIATION OF (A) YIELD STRESS, AND (B) PLASTIC VISCOSITY OF OWC SLURRIES AT DIFFERENT TEMPERATURES (DOSAGE OF ADMIXTURE = 0.5% BWOC).

order to predict the model's response within the range of the input data.

It can be observed that the yield stress for OWC slurries incorporating PCH was generally lower than that for slurries made with PCM and LSM. This is in agreement with findings for cement pastes [Al-Martini and Nehdi 2007, Al-Martini 2008]. Both the yield stress and plastic viscosity were found to be sensitive to the change in temperature; the higher the temperature the higher was the yield stress, which is in good agreement with experimental results.

The effect of the admixture dosage at different temperatures on the predicted rheological parameters of OWC slurries is illustrated in Fig. 13. Some admixture dosages not used in experiments were also included in model predictions. Both experimental and predicted values of yield stress decreased with PCH and PCM dosage. In the case of LSM, the predicted yield stress values increased with the dosage up to 1.5% and then started to decrease, which is in good conformity with experimental results. It can be observed that the variation of yield stress with admixture dosage was reasonably estimated for all the admixtures considered and its predicted values were comparable to the corresponding measured data.

Moreover, the plastic viscosity of OWC slurries was found to be sensitive to the change of temperature and admixture dosage (Fig. 13(b)). The plastic viscosity values predicted by both the ANN- and MRA-based models showed irregular behaviour, which may be associated with the error involved in fitting the curve to the Bingham model. It was argued [Al-Martini and Nehdi 2007] that plastic viscosity measured by fitting the down flow curve of the hysteresis loop to the Bingham model does not always truly represent the material properties because of the error associated with fitting the curve, which could be sometimes high as observed by Saak [2000].

Figures 12 and 13 reveal that the models were able to recognize and evaluate the effects of the admixture dosage and temperature on yield stress and plastic viscosity. The *AAE* of the ANN model predictions was in the range of 1.4 to 15.6% and 0.7 to 11.8% for yield stress and plastic viscosity, respectively, and that for the MRA model was in the range of 1.2 to 17.5% and to 1.3 to 14.5% for yield stress and plastic viscosity, respectively; depending on the admixture dosage and temperature tested. The higher values of *AAE* are usually associated with the lower yield stress and plastic viscosity values since small prediction errors may result in high *AAE* in such cases.

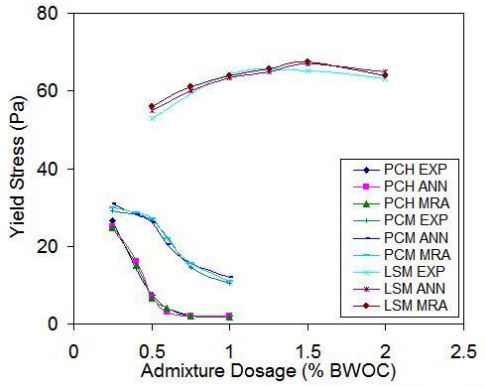

(A)

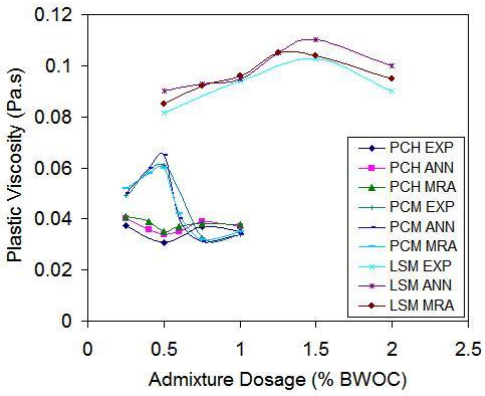

(B)

FIG. 13 VARIATION OF (A) YIELD STRESS, AND (B) PLASTIC VISCOSITY OF OWC SLURRIES WITH ADMIXTURE DOSAGE AND AT A TEMPERATURE OF 60°C.

8. Concluding Remarks

In this study, the relationships amongst the shear stress, shear rate, temperature, admixture type and dosage for OWC slurries have been analyzed. The

rheological properties of OWC slurries were modeled using a feed-forward back-propagation artificial neural network and multiple regression analysis. The models were then used to develop flow curves, which were used to calculate the yield stress and plastic viscosity values for OWC slurries with different admixtures and at different test temperatures. Based on this study, the following conclusions can be drawn:

- The ANN model developed in this study was able to learn the relationships between different shear flow parameters for various OWC slurries and successfully predicted their rheological properties of slurries used in the training process. It also demonstrated satisfactory performance when input parameters (shear rate, temperature, and dosage of admixture) unfamiliar to the ANN were used. The results prove that the ANN model is a powerful tool to quantitatively predict the rheological properties of OWC slurries within the range of tested admixture dosages and test temperatures.
- The MRA-based models were able to predict the rheological properties of OWC slurries with adequate accuracy.
- The flow curves developed using the ANN- and MRA-based models allowed predicting the Bingham parameters (yield stress and plastic viscosity) of OWC slurries with an acceptable accuracy and were found to be in good agreement with experimental results.
- The models proposed by both approaches were found to be sensitive to the effects of temperature increase and admixture dosage on the rheological properties of OWC slurries.
- The ANN-based model performed relatively better than the MRA-based model in predicting the rheological properties of OWC slurries.
- The proposed ANN- and MRA-based models can be extended and used to limit the number of laboratory trial mixtures and develop OWC slurries with suitable rheological properties, thus saving time and reducing the cost of OWC slurry design for specific applications.

REFERENCES

Al-Martini, S., and Nehdi, M., "Effect of Chemical Admixtures on Rheology of Cement Pastes at High Temperature," Journal of ASTM International, Vol. 4, No. 3, 2007, 17 p.

Al-Martini, S., "Investigation on Rheology of Cement Paste and Concrete at High Temperature," PhD Thesis, The University of Western Ontario, 2008.

Al Martini, S, and Nehdi, M., "Coupled Effects of Time and High Temperature on Rheological Properties of Cement Pastes Incorporating Various Superplasticizers," ASCE Journal of Materials in Civil Engineering, Vol. 21, No. 8, 2009, pp. 392-401.

ANSI/API RP 10B-2, "Recommended Practice for Testing Well Cements," 1st Edition, July 2005, 171 p.

Bruni, C., Forcellese, A., Gabrielli, F., and Simoncini, M., "Modelling of the Rheological Behaviour of Aluminium Alloys in Multistep Hot Deformation Using the Multiple Regression Analysis and Artificial Neural Network Techniques," Journal of Material Processing Technology, Vol. 177, No. 1-3, 2006, pp. 323-326.

Cohen, J., Cohen, P., West, S. G., and Aiken, L. S., (2003). "Applied Multiple Regression/Correlation Analysis for the Behavioral Sciences," 3rd Ed. Mahwah, NJ: Lawrence Erlbaum Associates, 2003, 736 p.

Demuth, H., Beale, M., and Hagan, M., "Neural Network Tool BoxTM 6 for Use with MATLAB R2008a," The Math Works Inc., Natick, Massachusetts, 2008, pp. 5.2 to 5.72.

El-Chabib, H., and Nehdi, M., "Neural Network Modelling of Properties of Cement-Based Materials Demystified," Advances in Cement Research, Vol. 17, No. 3, 2005, pp. 91-102.

El-Chabib, H., Nehdi, M., and Sonebi, M., "Artificial Intelligence Model for Flowable Concrete Mixtures Used in Underwater Construction and Repair," ACI Materials Journal, Vol. 100, No. 2, 2003, pp. 165-173.

Ferguson, J., and Kenblowski, Z., "Applied Fluid Rheology," Elsevier Applied Science, London and New York, 1991, pp. 209-210.

Genentech, "BioOncology Glossary," available online at http://www.gene.com/gene/news/kits/biooncology/oncologyterminology.html, accessed on July 13, 2010.

Guillot, D., "Rheology of Well Cement Slurries," Well Cementing, Edited by E.B. Nelson and Guillot, D. Schlumberger, Texas, 2006, pp. 93-142.

Health and Income Equity, Glossary, available online at http://depts.washington.edu/eqhlth/pages/academic_reso

urces/glossary.html#p, accessed on July 13, 2010.

Montgomery, D. C., Design and Analysis of Experiments, 7th Ed., Wiley, New York, 2009.

Ravi, K.M., and Sutton, D.L., "New Rheological Correlation for Cement Slurries as a Function of Temperature," SPE 20499, The 65th Annual Technical Conference and Exhibition of the Society of Petroleum Engineers, New Orleans, LA, Sept. 23-26, 1990, pp. 455-462.

Saak, W. A., Jennings, M. H., and Shah, P. S., "The influence of wall slip on yield stress and viscoelastic measurements of cement paste." Cement and Concrete Research, Vol. 31, n. 2, 2001, pp. 205–212.

Saak, W.A., "Characterization and Modeling of the Rheology of Cement Paste: With Application toward Self-Flowing Materials," Ph.D. Thesis, University of North Western, 2000.

Sonebi, M. "Factorial Design ModellingoOf Mix Proportion Parameters of Underwater Composite Cement Grouts," Cement and Concrete Research 31, No. 11, 2001, pp. 1553–1560.

Statsoft, Multiple Regression, Electronic Statistics Textbook, available online at http://www.statsoft. com/textbook /multiple-regression/, accessed on July 13, 2010.

Characterization of Multicrystalline Silicon Solar Wafers Fracture Strength and Influencing Factors

V.A. Popovich[1], A.C. Riemslag[1], M. Janssen[1], I.J. Bennett[2], I.M. Richardson[1]

Delft University of Technology, Department of Materials Science and Engineering, Delft, The Netherlands[1];

Energy Research Centre of the Netherlands, Solar Energy, PV Module Technology, Petten, The Netherlands[2]

Email: v.popovich@tudelft.nl

Abstract

Silicon wafer thickness reduction without increasing the wafer strength leads to a high fracture rate during subsequent handling and processing steps. Cracking of solar cells has also become one of the major sources of solar module failure and rejection. Hence, it is important to evaluate the mechanical strength of silicon solar wafers and factors influencing this. The purpose of this work is to understand the fracture behaviour of multicrystalline silicon wafers and to provide information regarding the bending strength of the wafers. The effects on silicon wafer strength of saw damage and of, grain size, grain boundaries and triple junctions are investigated. Also the effects of surface roughness and of the damage layer removal process are considered. Significant changes in fracture strength are found as a result of different silicon wafer crystallinity and surface roughness. It was found that fracture strength of the processed silicon wafer is mainly affected by the following factors: the thickness of the saw-damage layer (cracks length), surface roughness, cracks/defects at the edges and the amount of grain boundaries, serving as potential crack initiation points.

Keywords

Silicon Solar Cell; Fracture Strength

Introduction

Increases in silicon wafer size in combination with continuous wafer thickness reduction without strengthening the wafer leads to a high breakage rate during subsequent handling and processing steps and results in high costs [Popovich V.A; Brun X.F; Wang P.A]. It is well known, that silicon is a brittle material that is easy to break during the in-line process in which several loads are applied on the wafer surface and edges [Lawn B.R; Chen Po-Ying]. Cracking of silicon solar cells has become one of the major sources of solar module failure and rejection. It is essential for silicon wafers to posses maximum fracture strength as it improves the ability of the thin wafers to survive mechanical and thermal loads induced by handling and cell processing. Therefore, it is not only important to investigate the electrical properties of silicon solar wafers and cells, but also the mechanical properties, especially the strength. Compared to single crystalline silicon [Hull R; Luque S], relatively little work has been done to characterize the mechanical properties and fracture behaviour of multicrystalline silicon. Factors influencing strength and the mechanism of fracture have to be understood in order to minimize the fracture rate and to optimize the processing steps.

In this work the fracture strength is measured of silicon wafers by a four-point bending method. Results are statistically evaluated by a Weibull analysis, which provides information on the flaw distribution in the sample. Furthermore, Raman spectroscopy and confocal microscopy are used to further characterise the silicon wafers.

The purpose of this research is to determine the nature and source of the defects (flaws) controlling the fracture of multicrystalline silicon solar wafers and to provide information regarding the bending strength of wafers. The resulting data can be used to enhance production yields, improve cell reliability and establish mechanical criteria that lead to a reduction in cell costs. In this paper several aspects are described that affect mechanical strength, *i.e.* silicon wafer crystal structure, saw damage, and surface roughness.

Experimental Conditions

Material preparation

Bending tests were performed on rectangular multicrystalline (mc) silicon samples of 10 x 30 mm^2 with a thickness of 200 μm. These samples were laser-cut from neighbouring wafers, using a standard industrial

process, from the middle of one cast block, assuring a relatively low defect density. The edges of all specimens were polished down to a 1 μm finish and carefully examined under optical microscope.

Samples with specific types of crystallinity were prepared in order to investigate the effect of crystallinity features on the mechanical strength of the silicon wafer. In order to statistically evaluate the results, 15 neighbouring specimens (thus featuring the same crystallinity features) were prepared. The specimens were divided into 6 groups according to the crystallinity type in the centre of the specimen, see Figure 1, namely: one big grain, a twin boundary, a grain boundary perpendicular to the loading direction, several grains, a triple junction and many small grains.

To analyze the effect of surface roughness three types of specimens were prepared from neighbouring wafers, thus having the same crystallinity. The surface condition of these specimens included:

- The as-cut state, thus including the saw-damage layer.
- A surface textured by etching 30 s in a HF (10%) + HNO_3 (30%) + CH_3COOH (60%) solution. This serves two main purposes: to remove the damaged layer and to create a highly textured silicon surface in order to trap the light.
- A chemically polished surface (15 μm removal from both wafer sides in HF+HNO_3 bath for 1 min.).

Confocal microscopy was used to evaluate the obtained surface roughness profiles.

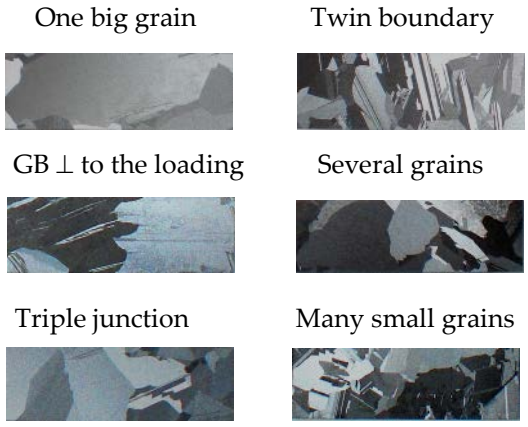

FIGURE 1 GROUPS OF SPECIMENS SHOWING TYPICAL CRYSTALLINITY FEATURES

Raman spectroscopy

The effects of saw damage removal were analyzed using Raman spectroscopy by comparing results from as-cut wafers with those from etched specimens. In all cases only neighbouring wafers were used. The Raman measurement was carried out at room temperature in the backscattering configuration. A Renishaw Raman spectrometer was used, equipped with a He-Ne laser with an excitation wavelength of 633 nm and a 100× objective, resulting in a focused spot with a diameter of ~1 μm and a penetration depth of a few μm in silicon. The measurement was performed in 3 accumulations with 5% of the total 50 W power. The c-Si TO peak was fitted to a Lorentzian distribution.

Raman spectroscopy gives information on the plane stress state in the outer surface layer (a few μm) of the silicon. In the technique used here, in which no polarised light is used, information is obtained on the average in-plane normal stress, σ. This information is contained in the wave number ω (inverse of wavelength) of the Raman peak. The value of σ relative to some reference state, Δσ, can be evaluated from the shift $\Delta\omega = \omega_s - \omega_0$, with ω_0 being the peak position in the reference state and ω_s the peak position of the stressed state. Discarding the effect of grain orientation on this effect, the following approximate relations hold for:

- a uniaxial stress state [Kimoto, K.]:

$$\Delta\sigma\ (\text{MPa}) = -500\ \Delta\omega\ (\text{cm}^{-1}) \quad (1)$$

- a biaxial state [Wolf de I.]:

$$\Delta\sigma\ (\text{MPa}) = -250\ \Delta\omega\ (\text{cm}^{-1}) \quad (2)$$

Thus a shift of the Si Raman peak towards lower wave numbers corresponds to tensile stress and vice versa. Note that if a biaxial stress state exists in the wafer, this will be reduced to a uniaxial state by cross-sectioning the wafer.

Considering the experimental resolution of ±0.1 cm^{-1}, stresses can be evaluated within ±20 MPa [Wolf de I.].

Strength measurement

The four-point bending test was chosen in this research because this type of loading results in a uniform bending moment along the central part of the specimen. Silicon is a crack-sensitive material and its failure is driven by tension rather than compression. Fracture mechanics predicts that fracture will initiate on the tensile side at the location where the largest surface or edge defect is present. Loading a significant part of the specimen length to uniform tension reduces the spread obtained in the strength results.

To a large extent the test configuration complies with ASTM standard C 1161-02c, which is on the measurement of the flexural strength of ceramic material at ambient temperature. The bending tests were performed using a 100 kN Instron 5500R tensile machine equipped with a 10 N load cell. During the test the load and crosshead displacement were recorded until fracture. The crosshead speed was set such that the outer-fibre strain rate in the specimen was of the order of 10^{-4} s^{-1}.

For this research, a new testing fixture was designed especially for the thin silicon specimens taken from wafers. The configuration of the testing fixture is shown in Figure 2. The test fixture had a loading span equal to half the support span (*i.e.* a four-point - ¼ point configuration) and was semi-articulating.

It should be noted, that loading and supporting rollers are fixed ∅ 1.0 mm cylinders. This deviates from ASTM standard C 1161, which prescribes that:

- The roller diameter should be approximately 1.5 times the specimen thickness. However, such a small diameter would not be very practical in this case.
- During the bending test the loading and supporting rollers should be free to rotate inwards and outwards respectively. The fixed configuration used in this work will inevitably introduce some friction between rollers and specimen.

In order to investigate possible effects of friction, three different types of rollers were considered: as received, polished down to 1 μm and covered with 300 μm thick PFTE foil. However, as a result of our observations, polished rollers were chosen in this research in order to minimize frictional constraints between rollers and specimen surface as much as possible.

The friction occurring at the loading rollers will induce a tensile stress in the central part of the specimen. It can be reasoned, that for the four-point bending configuration the ratio of this friction stress σ_f and the outer-fibre bending stress σ_b is equal to

$$\frac{\sigma_f}{\sigma_b} = \frac{4df}{3L} \qquad (3)$$

Where d = specimen thickness, f = friction coefficient between roller and specimen and L = support span. Considering the very low value for d/L in our set-up (0.0033), the resulting stress ratio will always be very small. Therefore the use of fixed rollers is not expected to affect the results.

Typical 4-point-bending load-displacement curves of silicon samples with different crystallinity features are shown in Figure 3. As can be seen, the curves are almost identical with the exception of the failure loads. They exhibit linear behaviour up to the failure point, so a linear elastic stress distribution is assumed over the specimen thickness. The outer fibre stress σ in a rectangular beam specimen loaded in the 4-point bending configuration used [ASTM standard C 1161-02c] is:

$$\sigma = \frac{3PL}{4bd^2}, \qquad (4)$$

where P = applied force and b = width of the specimen.

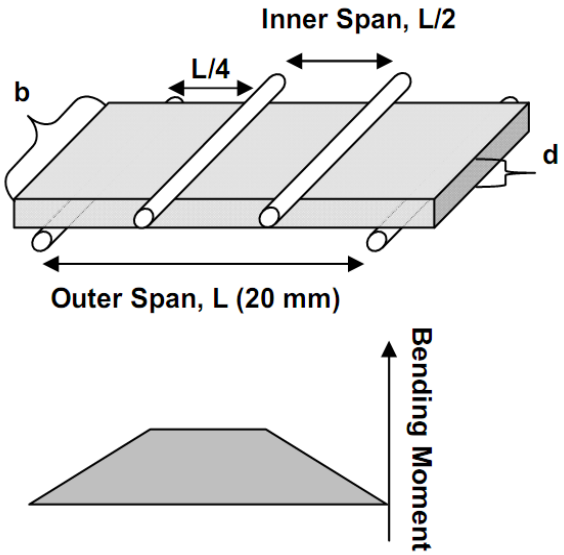

FIGURE 2 ILLUSTRATIONS OF THE FOUR-POINT BENDING TEST SETUP AND A CORRESPONDING BENDING MOMENT DIAGRAM

In order to prevent errors coming from the improper loading, load-displacement curves were closely monitored during the tests.

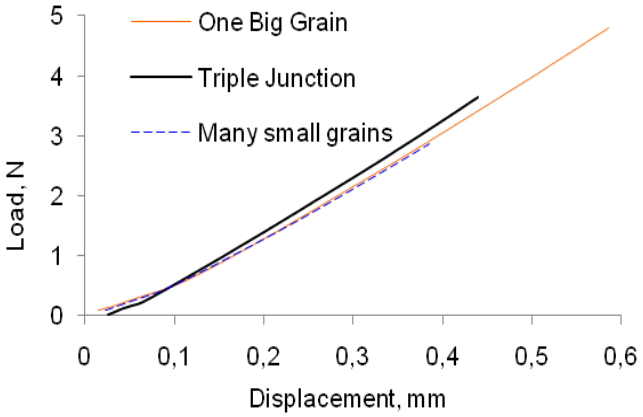

FIGURE 3 REPRESENTATIVE LOAD-DISPLACEMENT CURVES FOR SAMPLES WITH DIFFERENT CRYSTALLINITY

The strength of a brittle material such as silicon is de-

termined by the presence of defects that lead to crack initiation. A large scatter of the measured strength data will be observed, caused by the random distribution of defect location, size and orientation. Weibull statistics, based on the concept of the weakest link, is applied to describe the probability of failure by using two parameters [ASTM C 1239-95]:

$$P_f = 1 - \exp\left[-\left(\frac{\sigma}{\sigma_\theta}\right)^m\right] \quad (5)$$

where P_f is the probability of failure at an applied tensile stress σ, while σ_θ and m are the characteristic strength and the Weibull modulus of the specimen respectively. The characteristic strength, σ_θ, is the tensile stress at which 63.2% of all samples are expected to fail. The Weibull modulus, m, is a measure for the scatter of the measured strength values around the median strength. A large value stands for little scatter, which can be associated with a narrow defect distribution. Estimates for the Weibull parameters σ_θ and m, are found by making a plot of $\ln\{\ln[1/(1-P_f)]\}$ as a function of $\ln(\sigma)$. Data for this plot are obtained on the basis of experimental results on a sufficiently high number of similar specimens using the procedure described in [Weibull, W].

Results and Discussion

Effect of saw-damage on mechanical strength

Silicon specimens were cut using a conventional multi-wire-sawing process in order to see its influence on microstructure and mechanical strength.

Figure 4 represents a schematic illustration of wire saw cutting process. As can be seen, silicon cutting utilizes a steel wire, under high tension, that moves at high speed along the surface of the substrate. The wire is submerged in abrasive slurry, consisting of abrasive grit suspended in carbon fluid [Kao, I.]. When the abrasive particles are big, the damage of the Si surface is large and there are several large, deep grooves across the surface. The region near these grooves contains much damage and residual stresses.

Figure 5 shows a typical surface of an as-cut multicrystalline silicon wafer, containing large amount of smooth grooves. As-cut silicon samples were analyzed with a Raman spectrometer to investigate a nature of smooth grooves and to check for phase transformations in the damaged surface layer.

The Raman spectrum, shown in figure 6, clearly indicates the presence of amorphous Si (a-Si) next to polycrystalline Si on the as-cut surface. Many points at different positions on the wafer surface have been measured and in many of them a similar a-Si peak was found, either big or small.

As shown in figure 4, the microscopic silicon material removal process can be explained by the interaction of loose, rolling SiC particles that are randomly indented into the silicon surface until small crystal pieces are chipped away. Since SiC particles are facetted and contain sharp edges and tips, they can introduce very high local pressures on the surface [Gassilloud, R.].

It is known that when indented/scratched silicon, it locally induces a high pressure and silicon exhibits a phase transition from cubic diamond (Si-I) into a metallic (ductile) β-tin structure (Si-II). During the fast unloading this ductile phase in not stable and transforms into a layer of amorphous silicon or – if the unloading is slow enough – a mixture of amorphous and metastable phases (Si-XII- rhombohedral structure with 8 atoms per unit cell and Si-III phases *bc*8, body-centred cubic structure with 16 atoms per unit cell) is formed [Jang, J.-I; Kailer, A.].

In our study, the Si phase transition into amorphous silicon phase was found only in the smooth grooves (Figure 5). The rough parts of as-cut silicon wafer surfaces, where material is chipped off, mainly consist of stable crystalline silicon.

In order to see the influence of saw damage on the stress state and the mechanical strength of silicon wafers, 2 types of specimens were mechanically tested: as-cut specimens and specimens etched by an acidic solution to remove the damaged layer. The results, presented in Table 1, show that the as-cut specimens have a lower Weibull characteristic strength, σ_θ, which is presumably due to the presence of microcracks at the surface that is loaded in tension.

It is known that wafer strength is directly related to the density and the size of microcracks [Cook, R.F.; Gere, J.M.]. If density and size of microcracks are high, the probability that a macrocrack initiates and leads to failure for a given stress is also high.

Microcracks are induced during the sawing process while slicing the wafers from the ingot, which explains

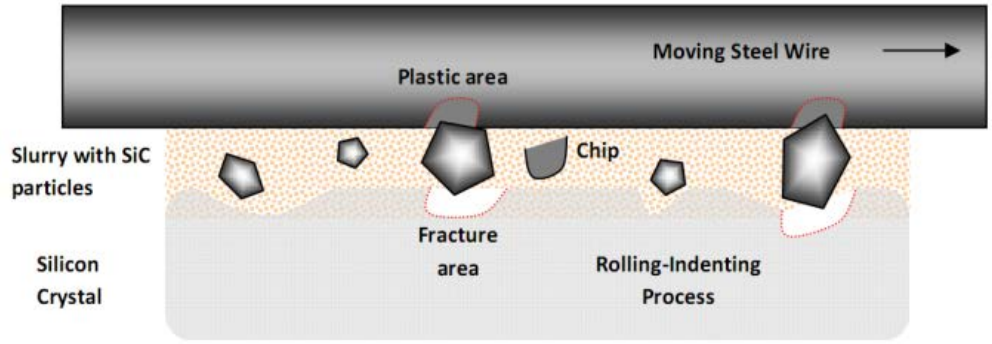

FIGURE 4 SCHEMATIC ILLUSTRATION OF THE ROLLING–INDENTING PROCESS IN THE WIRE-SAWING CUTTING PROCESS IN WHICH THE WIRE INTRODUCES FORCE ON THE ROLLING ABRASIVE SIC PARTICLES, THUS INDENTING THE CONTACT INTERFACE AND REMOVING MATERIALS FROM THE SURFACE

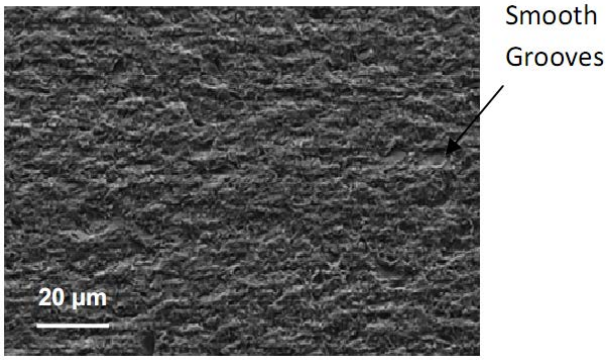

FIGURE 5 SCANNING ELECTRON MICROSCOPY MICROGRAPH OF A TYPICAL SURFACE OF THE AS-CUT MULTICRYSTALLINE SILICON WAFER

the lower strength in specimens in the as-cut state. Additionally, the presence of transformed a-Si phase could possibly also affect mechanical stability of the as-cut wafers.

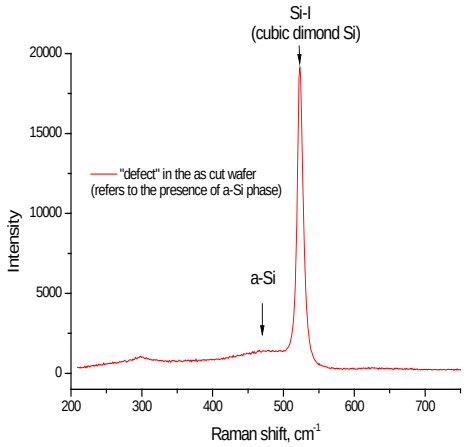

FIGURE 6 REPRESENTATIVE RAMAN SPECTRUM FOR THE AS-CUT WAFER SURFACE, SHOWING LOCAL INDENTATION-INDUCED TRANSFORMATION OF SI INTO AMORPHOUS SI

As a result of the etching process, the depth of surface microcracks is reduced, some cracks disappear completely and some crack tips become more blunted. Furthermore, the layer of transformed a-Si is removed. All these effects reduce the probability of macrocrack initiation, increasing the specimen strength.

In this work, Raman spectroscopy was also used to characterize the stress state in the damaged layer of the as-cut silicon wafer. As can be seen from Figure 7, there is a significant positive shift of the Raman peak for as-cut samples relative to the damage-free etched samples. This shift, $\Delta\omega$, of 2 cm^{-1} corresponds to a tensile stress of 500 MPa, assuming a biaxial stress state.

TABLE 1 EFFECT OF DAMAGED LAYER ON WEIBULL CHARACTERISTIC STRENGTH (σ_θ) AND MODULUS (m)

Surface condition	σ_θ (MPa)	m (-)
as-cut	155	9.4
after etching	234	8.3

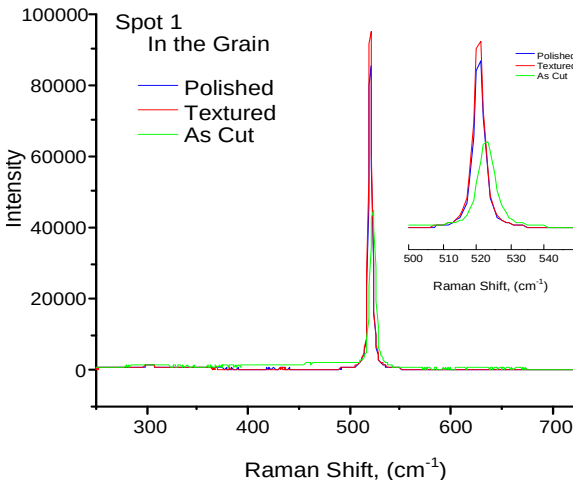

FIGURE 7 REPRESENTATIVE RAMAN SPECTRA OF THE AS-CUT, TEXTURED AND POLISHED NEIGHBOURING WAFERS

This stress value is representative only for the top few microns of the damaged layer, as this is the penetra-

tion depth of Raman Spectroscopy in silicon material.

Effect of surface roughness on mechanical strength

In this study, the as processed silicon wafers thickness remains the same, and the wafer edges are polished down to 1 μm. Therefore these factors will not influence the strength and the surface roughness completely determines the fracture strength of the multicrystalline silicon wafer specimens.

In order to investigate the effect of surface roughness on strength, three sets of specimens taken from neighbouring wafers (thus featuring the same crystallinity) with different surface conditions were tested, *i.e.* as cut, textured and polished down 15 μm. Figure 8 shows representative confocal microscopy surface roughness profiles, taken after the respective surface treatments in the same areas of the neighbouring samples.

Table 2 contains the determined roughness parameters *Sz* and *Sdr*. As can be seen, samples with a textured surface show a significantly higher surface roughness compared to the as-cut state, presumably due to the formation of etch pits. It should also be noted, that etching/texturing creates a much rougher surface at the grain boundaries, probably due to local preferential etching (etched sample in Figure 8a).

The low value of Weibull modulus for the textured samples (m = 8.3; see Table 2) shows that apparently there is much variation in the size of the largest defects present at the tensile surface. However, despite the increase of the surface roughness, there is an increase of 50% in the characteristic strength as a result of the etching/texturing, probably due to the removal of the damaged layer.

Thus, it is suggested, that the size of microcracks in the damaged layer is a more dominant factor affecting mechanical strength of silicon wafers than the surface roughness.

Polishing the silicon wafers showed the expected reduction in surface roughness, as well as a significant increase in fracture strength (Table 2). A larger Weibull modulus, as compared to the as-cut and the textured state, indicates that the polishing process gives a much smoother silicon surface and a narrower defect distribution.

It can be concluded that, as long as saw-damage is removed, the surface roughness profile is the second most detrimental factor affecting mechanical strength of silicon wafers.

It can also be concluded, that the fracture strength of polished and textured silicon wafers is inversely proportional to the surface roughness, correlated as: $F_s \sim 1/R_a$, where F_s is fracture strength and R_a is surface roughness profile.

Effect of mc-silicon wafer crystallinity on mechanical strength

Specific types of silicon wafers crystallinity were chosen for this research to investigate the effect on mechanical strength. All specimens were etched by an acidic solution for 30 s to remove the damaged layer induced by the sawing process. The four-point bending strength was analyzed by Eg. (4). The results are given in Table 3, which lists the Weibull characteristic strength (σ_θ) and the Weibull modulus (m) of 15 tests.

As can be seen from Table 3, it is possible to define three main characteristic groups, based on the strength results. The specimens with one big grain in the middle have a much higher strength than those with many small grains in the middle. The four other crystallinity types, all having several grains in the middle, have intermediate strengths.

As for most brittle materials, the fracture strength of an

TABLE 2 EFFECT OF SURFACE ROUGHNESS PARAMETERS ON BENDING STRENGTH AND WEIBULL PARAMETERS OF MULTICRYSTALLINE SILICON WAFERS

Silicon Surface Treatment	In the Grain		Grain Boundary		σ_θ (MPa)	m (-)
	Sz	*Sdr*, %	*Sz*	*Sdr*, %		
As Cut	5.70	14.6	6.11	12.2	160	9.4
Textured	12.7	28.2	13.7	45.8	240	8.3
Polished	9.73	10.8	10.6	10.0	285	10.1

Sz is an average difference between the 5 highest peaks and 5 lowest valleys; *Sdr* is the developed Interfacial Area Ratio, which is expressed as the percentage of additional surface area contributed by the texture as compared to an ideal plane the size of the measurement region.

TABLE 3 EFFECT OF CRYSTALLINITY TYPE OF ETCHED WAFERS ON MECHANICAL STRENGTH

Crystallinity type	σ_θ (MPa)	m (-)
One big grain	287	7.9
Twin boundary	256	8.6
Triple junction	255	5.9
GB perpendicular to the loading direction	241	8.4
Several grains	228	5.5
Many grains	208	5.7

mc-silicon wafer depends on both material-intrinsic properties, such as grain size, grain boundaries and crystal orientation, and on extrinsic variables such as flaws and microcracks [Moller, H.J.].

The strength reduction due to the presence of many small grains might be related to the number of grain boundaries, which is proportional to the number of grains. Alternatively the surface roughness might be different for different crystallinity types, due to preferential etching of the grain boundaries. Surface roughness parameters of the three main crystallinity groups are given in Figure 9. As can be seen, there again seems to be a correlation between surface roughness and the fracture strength: the higher the surface roughness, the lower the fracture strength, Figure 9c.

In order to eliminate the effect of surface roughness, samples with crystallinity features similar to those shown in Figure 1 were polished to further reduce the surface roughness. As can be seen from Table 4, polishing the samples, leads to higher Weibull characteristic strengths and moduli, probably due to a reduction of the roughness at the grain boundaries.

TABLE 4 EFFECT OF CRYSTALLINITY TYPE OF POLISHED WAFERS ON MECHANICAL STRENGTH

Crystallinity type	σ_θ (MPa)	m (-)
One big grain	293	8.5
Twin boundary	274	8.9
Triple junction	268	6.7
GB perpendicular to the loading direction	266	9.1
Several grains	260	7.4
Many grains	251	6.9

It should be pointed out, that a significant increase of strength is only observed in samples with many grains, which can be related to the levelling off (by the polishing) of etch pits that were formed near the grain boundaries during the texturing/etching process.

Nonetheless, samples with polished surfaces show the same correlation between crystallinity and fracture strength, namely, the higher the number of grain boundaries the weaker the sample is. Furthermore, fracture patterns of the polished silicon samples subjected to 4-point bending revealed a preferential propagation of the cracks along the grain boundaries (Figure 10).

It should be pointed out, that a significant increase of strength is only observed in samples with many grains, which can be related to the levelling off (by the polishing) of etch pits that were formed near the grain boundaries during the texturing/etching process.

Nonetheless, samples with polished surfaces show the same correlation between crystallinity and fracture strength, namely, the higher the number of grain boundaries the weaker the sample is. Furthermore, fracture patterns of the polished silicon samples subjected to 4-point bending revealed a preferential propagation of the cracks along the grain boundaries (Figure 10).

From these results it can be concluded, that for polished silicon wafers crystallinity is the most significant factor affecting the strength, probably due to a lower strength of grain boundaries leading to intergranular fracture of the polished multicrystalline silicon samples. On the other hand, there is a mixed type fracture (transgranular and intergranular) for textured and as-cut silicon wafers, where surface roughness and a damaged surface layer are the most detrimental factors.

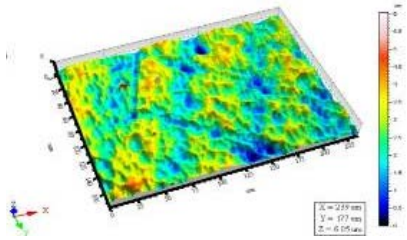

a)

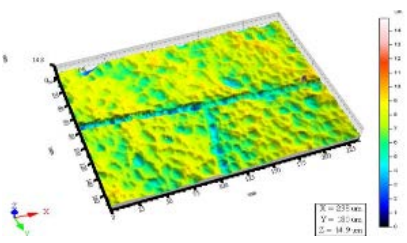

b)

Crystallinity type	*Sz* (μm)	*Sdr* (%)	σ_θ (MPa)
One big grain	7.5	5	287
Triple junction	13	25	255
Many small grains	11	27	208

c)

FIGURE 9 REPRESENTATIVE SURFACE ROUGHNESS PROFILES OF ETCHED SAMPLES: A) ONE BIG GRAIN, B) TRIPLE JUNCTION AND C) SURFACE ROUGHNESS PARAMETERS AND CHARACTERISTIC STRENGTHS

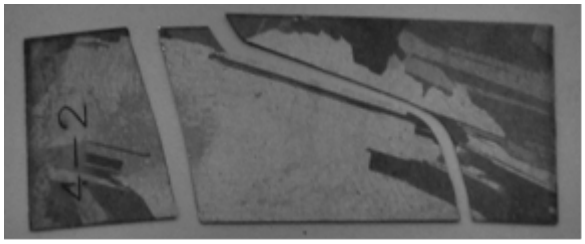

FIGURE 10 EXAMPLE OF THE FRACTURE PATTERN OF A POLISHED MC-SILICON SAMPLE, SHOWING DEFLECTION OF THE CRACK ALONG THE GRAIN BOUNDARY

Conclusions

The mechanical strength of multicrystalline (mc) silicon solar wafers was investigated using four-point bending tests.

Raman spectroscopy was used to characterise the wafer surfaces. The study showed that:

- The surface layer damaged by the sawing process contains a mixture of indentation-transformed amorphous silicon and a stable crystalline silicon phase;
- The top few microns of the damaged layer contains tensile stresses in the order of 500 MPa (compared to neighbouring damage-free wafers);
- Damage layer removal by etching increases the strength of the mc-silicon wafer by about 50%;
- Samples with removed damaged layer show an inverse proportionality between the surface roughness profile and the fracture strength;
- Mc-silicon wafer crystallinity has a significant effect on the mechanical strength of polished multicrystalline silicon wafers;
- Surface and edge defects, such as microcracks, grain boundaries and surface roughness are the most probable sources of mechanical strength degradation; reduction of microcracks leads to an increase of the fracture strength of a mc-silicon wafer;
- Results suggest, that there is a mixed type fracture (transgranular and intergranular) for as-cut and for textured silicon wafers. For polished silicon wafers, however, crystallinity is the most significant factor affecting the strength, suggesting a relative weakness of the grain boundaries, leading to an intergranular fracture mode.
- Further than 15 microns mechanical polishing of silicon wafers could further increase fracture strength and result in a reduction of costs.

REFERENCES

ASTM Standard C 1161-02c, Standard Test Method for Flexural Strength of Advanced Ceramics at Ambient Temperature, ASTM International, West Conshohocken, USA, 2008.

ASTM C 1239-95. Reporting Uniaxial Strength Data and Estimating Weibull Distribution Parameters for Advanced Ceramics, 1995.

Brun, X.F., Melkote, S.N., Analysis of stresses and breakage of crystalline silicon wafers during handling and transport, Solar Energy Materials and Solar Cells, Volume **93**, 2009, pp. 1238–1247.

Chen, Po-Ying, Tsai, Ming-Hsing, Relationship between wafer edge design and its ultimate mechanical strength, Microelectronic Engineering, Volume **87**, Issue 11, November 2010, pp. 2065-2070

Cook, R.F., Strength and sharp contact fracture of silicon, J. Mater. Sci. **41**, 2006.

Gassilloud, R., Ballif, C., et. al, Deformation mechanisms of silicon during nanoscratching, Phys. stat. sol. (a) 202, No. **15**, 2005, pp. 2858–2869.

Gere, J.M., Goodno, B. J., Mechanics of Materials, seventh ed., Cengange Learning, USA, 2009.

Hull R. Properties of Crystalline Silicon, Chapter 3, Structural and Mechanical properties (edited by A. George). INSPEC, London, 1999

Jang, J.-I., Lance, M.J., Indentation-induced phase transformations in silicon: Influences of load, rate and indenter angle on the transformation behaviour. Acta Mater. **53(6)**,

2005, pp. 1759–1770

Kailer, A., Gogotsi, Y.G., Nickel, K.G., Phase transformations of silicon caused by contact loading. J. Appl. Phys. **81(7**), 1997, pp. 3057– 3063

Kao, I., Wei, S., Chiang, F.-P.: Vibration of wiresaw manufacturing processes and wafer surface measurement, NSF Des. Manuf. Grantees Conf., Monterey, 1998, pp. 427–428

Kimoto, K., Usami, K., Japan. *J. Appl. Phys.* **32,** 1993, pp. 211–213.

Lawn, B.R., Fracture of Brittle Solids, Cambridge University Press, 1993.

Luque, S. Hegedus, "Handbook of Photovoltaic Science and Engineering", John Wiley & Sons Ltd, West Sussex, England, 2003.

Moller, H.J., Funke, C., Rinio, M., Scholz, S., Multicrystalline silicon for solar cells, Thin Solid Films, Volume **487**, Issues 1-2, International Conference on Polycrystalline Semiconductors- Materials, Technologies, Device Applications, 1 September 2005, pp. 179-187.

Popovich, V.A., Yunus, Janssen, A., M., Richardson, I.M., Bennett, I.J., Effect of silicon solar cell processing parameters and crystallinity on mechanical strength, Solar Energy Materials and Solar Cells, Volume **95**, Issue 1, PVSEC-19, Jeju, Korea, 9-13 November 2009, January 2011, pp. 97-100.

Wang, P.A., Industrial challenges for thin wafer manufacturing, in: Proceedings of the Fourth World Conference on Photovoltaic Energy Conversion, Waikoloa, HI, USA, 2006, pp. 1179–1182.

Weibull, W., A statistical distribution function of wide applicability, *J. Appl. Mech.* **18**, 1951, pp. 293–297.

Wolf, I. De, "Micro-Raman spectroscopy to study local mechanical stress in silicon integrated circuits", *Semicond. Sci. Technol.* **11**, 1996, pp. 139-154.

The Sorption Properties of Exploding Wire Prepared Ag, Fe and ZnO Nanoparticles for Nitrite Removal from Water

Abdullah Alqudami*[1], Saqr Munassar[1], Nabil Alhemiary[2]

[1]Department of Physics, Faculty of Science, University of Ibb, P.O. Box 70270, Ibb, Yemen

[2]Department of Chemistry, Faculty of Science, University of Ibb, P.O. Box 70270, Ibb, Yemen

*alqudami@gmail.com

Abstract

Part of the research work carried out at our university is presented. Ag, Fe and ZnO nanoparticles are prepared by the lab made electro-exploding wire system. The prepared nanoparticles are utilized in water pollution treatment. Laboratory experiments have been designed for exploring the sorption properties of these nanoparticles for the removal of nitrite from water. Spectrophotometric method was used for the determination of nitrite in the concentration range of 0.05–2.5 mg/L. At fixed concentrations of nitrite and nanoparticles (2.5:1.6) mg/L (nitrite: nanoparticles), It was observed that Ag nanoparticles possess highest sorption capability for removing nitrite followed by Fe nanoparticles. The calculated equilibrium adsorption capacities (q_e) were 980, 603 and 376 mg/g (adsorbate/adsorbent) for the nitrite sorption onto Ag, Fe and ZnO nanoparticles, respectively. The adsorption kinetic data were analyzed using the pseudo first-order, pseudo second-order and intraparticle diffusion model. Ag, Fe and ZnO nanoparticles exhibited excellent efficiencies for removing nitrite from water.

Keywords

Exploding Wire; Nanoparticles; Nitrite Sorption; Water Treatment

Introduction

Most nitrogenous materials in natural waters tend to be converted to nitrate, so all sources of combined nitrogen, particularly organic nitrogen and ammonia, should be considered as potential nitrate sources. Primary sources of organic nitrates include human sewage and livestock manure, especially from feedlots. The primary inorganic nitrates which may contaminate drinking water are potassium nitrate and ammonium nitrate both of which are widely used as fertilizers.

Nitrates themselves are relatively nontoxic. However, when swallowed, they are converted to nitrites that can react with hemoglobin in the blood, oxidizing its divalent iron to the trivalent form and creating met-hemoglobin. This met-hemoglobin cannot bind oxygen, which decreases the capacity of the blood to transport oxygen so less oxygen is transported from the lungs to the body tissues, thus causing a condition known as met-hemoglobinemia. Met-hemoglobinemia occurs mostly in children and is also known as ''blue-baby syndrome'' (Shuval and Gruener 1977; Kapoor and Viraraghavan 1997).

Consequently, the concentration of nitrate and nitrite in drinking water has been regulated. The levels in drinking water of nitrate and nitrite established by the European Union legislation are 50 and 0.5 mg/L, respectively (Council Directive 1991). In the United States, EPA (2003) establishes the maximum contaminant levels of 10 mg/L for nitrate and1.0 mg/L for nitrite in public water supplies.

Nitrate-contaminated waters are commonly treated by ion exchange or reverse osmosis. However, these traditional treatments are relatively expensive, because they require frequent regeneration of the media, or generate secondary brine wastes that may pose a disposal problem. Biological denitrification (Kim, Seagren, and Davis 2003; Davis 2007) is another alternative to remove nitrate from water because the microbial process reduces the nitrate to innocuous nitrogen gas rather than ammonium and generally results in lower operating costs as compared to ion exchange or reverse osmosis. However, this process can produce excessive biomass and soluble microbial products that require further treatment of the denitrified water (aeration and disinfection). Moreover, the denitrification process is generally slow and sometimes incomplete as compared to chemical reduction. The catalytic hydrogenation of nitrate (Horold et al. 1993; Gavagnin et al. 2002) is suitable for fast treatment of the nitrate-contaminated water but still requires an addition of a reducing agent (such as

hydrogen). In recent years, the success of iron metal in treating groundwater containing chlorinated solvents has stimulated a significant interest in the application of zero-valent iron (Maroto et al. 2009; Suzuki et al. 2012). However, nitrate reduction by Fe^0 is relatively sensitive to the solution pH, and nitrate is well known as an oxidizing inhibitor to iron corrosion due to the formation of an overlying oxide layer.

Sorption, in general, is the process of collecting soluble substances that are in solution on a suitable interface. The most efficient and commonly used adsorbent is activated carbon (Lee, Low, and Chung 1997; Wang et al. 2006). However, Activated carbon is very expensive adsorbent for removal of pollutant therefore other adsorbent must be investigated.

Nanoparticles (NP) could be an additional alternative option as a metal contaminant sorbent. Larger surface area may translate into greater sorption capacities allowing for smaller sorbent volumes and less waste for disposal. As particle size decreases more unsaturated surface atoms are exposed prompting greater reactivity. For example, nanoscale iron particles were employed for the denitrification of unbuffered nitrate solutions at initial neutral pH (Liou et al. 2005).

We have been working with the preparation of pure metallic Ag and Fe NP using a novel electro-exploding wire (EEW) technique (Sen et al. 2003; 2004; 2007). These NP exhibited interesting optical and magnetic properties (Alqudami and Annapoorni 2005, 2007; Alqudami et al. 2007, 2008; Sing, Alqudami, and Annapoorni 2010). The EEW technique is a direct & simple physical process and does not involve any chemical agent. Recent investigation showed that Ag and Fe NP prepared by EEW technique were effective adsorbents for the removal of Pb(II) and Cd(II) ions from water with high adsorption capacities at equilibrium (Alqudami, Alhemiary, and Munassar 2011).

This work aimed at investigating the adsorption behavior of Fe, Ag, and ZnO NP for the removal of nitrite from water. For this purpose, spherical Ag, Fe, and ZnO NP were prepared using EEW technique. The structural properties of these NP are published elsewhere (Alqudami and Annapoorni 2005, 2007; Alqudami et al. 2007, 2008; Sing, Alqudami, and Annapoorni 2010; Alqudami, Alhemiary, and Munassar 2011). The nitrite removal from water is investigated as functions of NP type and contact time. The adsorption properties are studied from kinetic standpoint.

Experimental

Nanoparticles Preparations

Prior to the performing experiments, Ag, Fe, and Zn wires (dia: 0.25 mm; Purity: 99.998%; Alfa Aesar) and plates (dim: 20, 20, 1 mm; Purity: 99.998%; Alfa Aesar) were cleaned using emery paper and followed by Acetone. The wires each of 20 mm length were exploded on plates of the same material type in distilled water using the EEW set-up sketched in Fig. 1. These wires have been exploded by bringing the metal wire into sudden contact with the metal plate. The above mentioned length of wire is standing for several sparks and is being replaced after several contacts. Both the electrodes (wire and plate) are subjected to a potential difference of 36 V DC supplied from three 12 V batteries connected in series. The resulted NP remain suspended in water (colloidal form). Independent experiments were performed to prepare each type of the NP. These NP were used to investigate their adsorption properties for the nitrite removal experiments.

The EEW process is very energy intensive since only relatively low voltages are applied, and also results in large quantities of NP being produced from both the consumed electrodes.

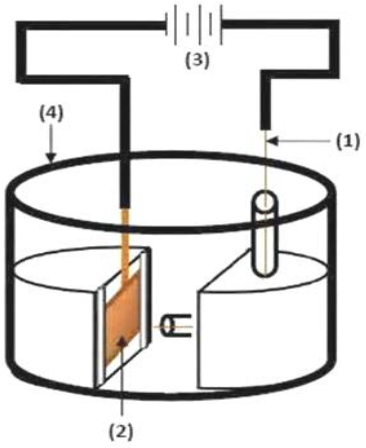

FIG. 1 A SCHEMATIC DIAGRAM OF THE ELECTRO-EXPLODING WIRE (EEW) SET UP; (1) THIN METAL WIRE, (2) METAL PLATE, (3) 36 V BATTERIES AND (4) GLASS VESSEL

Nitrite Ions Preparation

Chemicals used were of analytical grade and double distilled water was used throughout the experiments. Nitrite standard solution was prepared by dissolving 1.50 g of dried $NaNO_2$ in distilled water and diluting to the mark in a one-liter volumetric flask. Working solutions were prepared by appropriate dilution of the stock solution with water. A 0.04 M sulfanilic acid

solution was prepared by dissolving 1.7319 g of sulfanilic acid in water and diluting to the mark in a 250-mL volumetric flask. Acetic acid solution (6 M) was prepared by appropriate dilution of glacial acetic acid with water. A 0.5 M N,N-dimethylaniline solution was prepared by dissolving 6.3 mL N,N-dimethylaniline in water containing 20 mL of glacial acetic acid and diluting to 100 mL with distilled water. This solution was stored in a dark bottle in a refrigerator.

Determination of Nitrite Ions

A simple, rapid and sensitive spectrophotometric method was used for the trace determination of nitrite in water (Afkhami and Mogharnesband 1997; Aydin, Ercan, and Tascioglu 2005; Nagaraja, Prakash, and Bhaskara 2006).

All measurements were performed using 10-mL standard flask, containing 0.5-25 μg of nitrite along with 0.6 mL of 0.5 M N,N-dimethylaniline and dilute to the mark with water. The solutions were shaken on a rotary shaker for fixed periods and then were centrifuged at speeds of 6000 rpm for 5 minutes to remove the precipitated solid and then filtered using filter papers. 3 mL from the solution were transferred into quartz cells for measuring the absorbance at 510 nm using a Shimadzu model UV-120-01 spectrophotometer. The absorbance at 510 nm are measured in 1.00 cm quartz cells against reagent blank which is prepared in the same manner but in the absence of nitrite.

Under the optimum conditions, a calibration graph is plotted for nitrite as in Fig. 2. A straight line has been obtained in the concentration range of 0.05 – 2.5 mg/L, with a correlation of 0.99 and a regression equation of,

$$\mathbf{A} = 0.07199 + 0.35402\ \boldsymbol{C}$$

Where ***C*** is the concentration of nitrite in mg/L

Kinetics of the Nitrite Ions Sorption

All measurements were performed using 10-mL standard flask, containing 25 μg of nitrite and 16 μg of nanoparticles along with 0.6 mL of 0.5 M N,N-dimethylaniline and dilute to the mark with water.

The 10-mL solutions (nitrite + nanoparticles + methyl orange in acidic media) with fixed concentrations of nitrite and nanoparticles (2.5:1.6) mg/L (nitrite: nanoparticles) were shaken on a rotary shaker for different periods, namely for 5, 10, 20, 30 and 60 minutes. Then, the solutions were centrifuged at speeds of 6000 rpm for 5 minutes to remove the precipitated solid and filtered using filter papers. 3 mL from the decanted solutions were transferred into quartz cells for measuring the absorbance at 510 nm during the first 5 minutes by using a spectrophotometer. The concentration of nitrite ions were calculated as a function of nanoparticle type and contact time. The sorbed amount was calculated as the difference between the nitrite contents of the final solutions and control samples in the absence of nanoparticles. All experiments were performed at room temperature (30 °C).

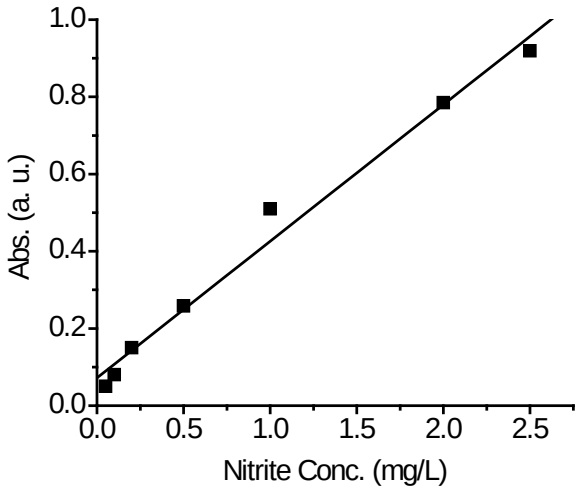

FIG. 2 A CALIBRATION GRAPH FOR NITRITE ABSORBANCE VERSUS CONCENTRATION

Results and Discussion

Effect of NP Type and Contact Time

The removal of nitrite by several adsorbents namely Ag, Fe, and ZnO NP are shown in Fig. 3 & Fig. 4.

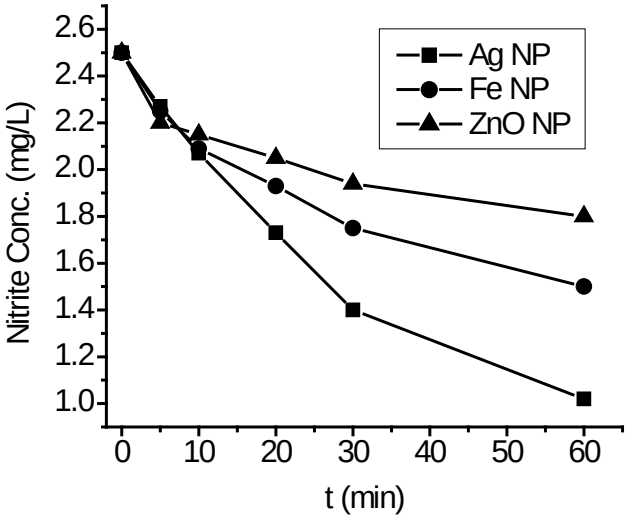

FIG. 3 ADSORPTION OF NITRITE BY Ag, Fe, AND ZnO NP AS A FUNCTION OF CONTACT TIME IN MINUTES

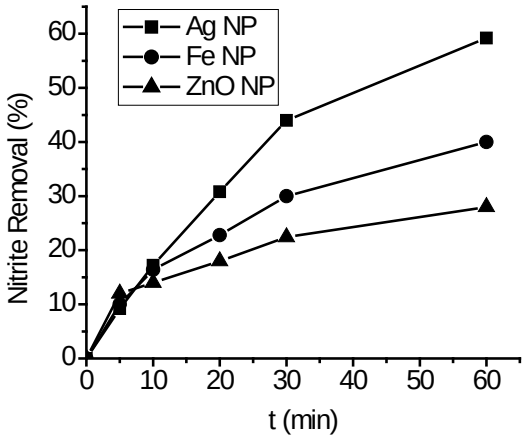

FIG. 4 REMOVAL OF NITRITE BY Ag, Fe, AND ZnO NP AS A FUNCTION OF CONTACT TIME IN MINUTES

Although NP concentrations were about one half of the nitrite concentration, the NP show remarkable removal efficiencies. 60% of the nitrite ions were removed in 60 minutes of contact with Ag NP. The removal efficiency was less by using Fe and ZnO NP at the same time of contact. The removal of nitrite was rapid in the initial stages of contact time and slowly increased with lapse of time. The variation of removal efficiency might be due to the formation of oxide shell around Fe NP and due to full oxidation of Zn NP (will be discussed in more detail on page 34).

Adsorption Kinetics

Many mathematical models are reported in the literature, all attempting to describe quantitatively the kinetic behavior during the adsorption process. Among these, the pseudo-first-order (Lagergren 1898; Ho 2004) and pseudo-second-order (Ho et al. 2000) models were used to test kinetic experimental data;

$$\frac{d\,q_t}{dt} = k_1\,(q_t - q_e) \qquad (1)$$

$$\frac{d\,q_t}{dt} = k_2\,(q_t - q_e)^2 \qquad (2)$$

where, q_e and q_t are the amounts of nitrite adsorbed (mg/g) per unit weight of adsorbent at equilibrium and at time t (min), respectively, k_1 and k_2 are reaction rate constants. The following linearised time dependent functions were obtained by integrating and rearranging Eq. 1 and Eq. 2 with the boundary conditions of $t = 0$ and $q_t = 0$ to $t = t$ and $q_t = q_e$ to yield;

$$log(\,q_e - q_t\,) = log\,q_e - \frac{k_1}{2.303}t \qquad (3)$$

$$\frac{t}{q_t} = \frac{1}{k_2\,q_e^{\,2}} + \frac{t}{q_e} \qquad (4)$$

Plots of $log(q_e - q_t)$ versus t and of t/q_t versus t are presented in Fig. 5 and Fig. 6, respectively.

Values of k_1, k_2 and q_e were calculated from the intercept and slope of the plots of $\log(q_e - q_t)$ vs. t, and t/q_t vs. t, and all are listed in Table 1. The results showed that the pseudo-first-order rate expression was valid for the adsorption of nitrite onto Ag NP and Fe NP. The experimental q_e values are in agreement with the calculated ones, obtained from the linear plots (Table 1) and the correlation coefficient values are higher when compared to those obtained using the pseudo-second-order rate expression for the same adsorbents. However, the adsorption of nitrite using ZnO NP showed to follow the pseudo-second-order rate equation due to relatively high value of correlation coefficient (Table 1).

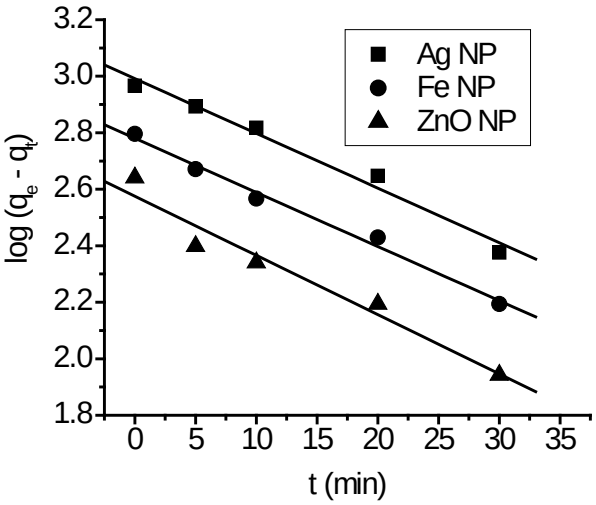

FIG. 5 APPLICATION OF THE PSEUDO FIRST-ORDER KINETIC MODEL TO THE ADSORPTION OF NITRITE

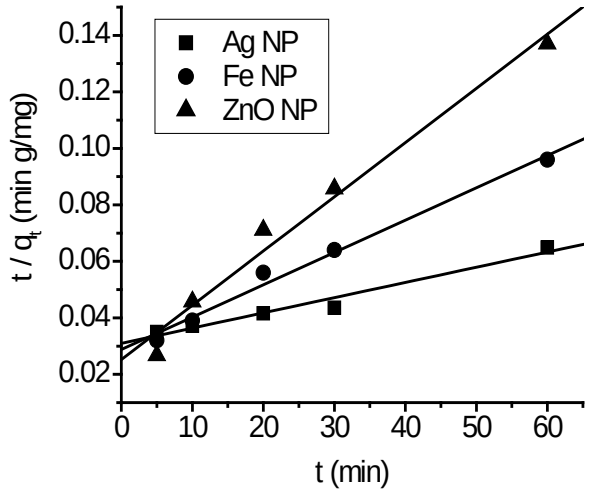

FIG. 6 APPLICATION OF THE PSEUDO SECOND-ORDER KINETIC MODEL TO THE ADSORPTION OF NITRITE

TABLE 1 NITRITE ADSORPTION KINETICS

Adsorbent NP	q_e (Exp) (mg/g)	Pseudo First-Order			Pseudo Second-Order			Intraparticle Diffusion	
		q_e (mg/g)	k_1 (min^{-1})	R^2	q_e (mg/g)	k_2 (g/mg min)	R^2	k_i (mg/g $min^{1/2}$)	R^2
Ag	925	980	0.0446	0.9817	1856	9.37 x10^{-6}	0.9691	114	0.9867
Fe	625	603	0.0441	0.9905	877	45.2 x10^{-6}	0.9883	81.3	0.9927
ZnO	438	376	0.0483	0.9562	520	147 x10^{-6}	0.9799	61.4	0.9911

Intraparticle Diffusion Model

Adsorption is a multi-step process involving transport of the sorbate from the bulk solution to the surface of the sorbent, followed by intraparticle or pore diffusion, where sorbate move into the interior of sorbent particles, and adsorption on the interior sites of the sorbent (Bhattacharyya and Sharma 2004). The intraparticle diffusion equation can be described as:

$$q_t = k_i t^{1/2} + c \qquad (5)$$

where k_i is the intraparticle diffusion rate constant (mg/g $min^{1/2}$). The k_i is the slope of straight line portions of the plot of q_t vs. $t^{1/2}$.

According to this model, a plot of q_t versus $t^{1/2}$ should be linear if intraparticle diffusion is involved in the adsorption process and if the plot passes through the origin then intraparticle diffusion is the sole rate-limiting step (Ozcan, Ozcan S, and Gok 2007). It has also been suggested that in instances when q_t versus $t^{1/2}$ is multilinear, two or more steps govern the adsorption process (Unuabonah, Adebowale, and Olu-Owolabi 2007; Wu, Tseng, and Juang 2009).

Fig. 7 shows the plots of q_t vs. $t^{1/2}$ for the adsorption of nitrite onto Ag, Fe and ZnO NP.

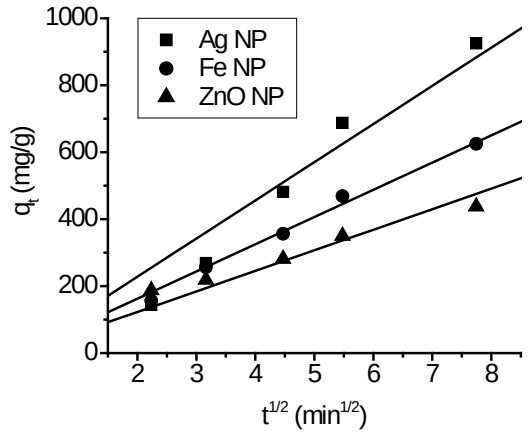

FIG. 7 INTRAPARTICLE DIFFUSION MODEL FOR THE SORPTION OF NITRITE ONTO Ag, Fe, AND ZnO NP

Given the linear plots of q_t vs. $t^{1/2}$ for the adsorption of nitrite on Ag, Fe and ZnO NP, this suggests that intraparticle diffusions are involved in the adsorption processes. The intraparticle diffusion rate constants k_i were calculated from the slopes of the straight lines and are shown in Table 1 along with the correlation coefficients. As the plots did not pass through the origin, intraparticle diffusions were not the only rate-limiting step. The values of the intercept *c* provide information related to the thickness of the boundary layer (Kavitha and Namasivayam 2007). Larger intercepts suggest that surface diffusion has a larger role as the rate-limiting step.

Further Discussion

To understand the sorption properties of the EEW prepared Ag, Fe, and ZnO NP, it is important to discuss the processes of NP formation using EEW technique. During NP production by under-water wire explosions, water decomposition (e.g. electrolysis) may occur. This would result in the generation of gaseous hydrogen and oxygen. Hydrogen and oxygen start to interact with the newly prepared NP. Since hydrogen (molecular or atomic forms) does not adsorb on Ag, Fe and Zn particle surfaces at room temperature (Dus and Nowicka 2003) and also is not significantly dissolved in water, it is ultimately removed to the gas phase. However, oxygen (especially atomic) could adsorb and react with the Ag, Fe and Zn surfaces at room temperature. It is also expected that during the EEW process, electrons are injected from the cathode to the NP, additionally saturated by atomic oxygen. Hence, Ag as well as Fe clusters could easily create hydrogen bonds with water particles in water environments. Finally, negatively charged Ag and Fe NP are created in the water medium due to the formation of thin oxides/hydroxyl layer around the spherical metallic core (Alqudami, Alhemiary, and Munassar 2011). Earlier investigation showed that the presence of dissolved oxygen in water is playing a key role in the

complete conversion of Zn to ZnO phase (Singh, Alqudami, and Annapoorni 2010). It is likely that the dissolved oxygen molecules are diffusing into the Zn particle slowly and reacting with the Zn atoms to form ZnO nanocrystals. Here, it is interesting to note that metal-to-metal oxide seems to depend on the properties like reactivity to oxygen and melting point.

During the adsorption experiments in acidic media, it was believed that acid dissolves the oxide passive layers at low pH, and as a result, the regenerated metallic core or active metallic sites are exposed to nitrite ions. Metallic core surface (M^0) then will effectively adsorb and reduce NO_2^-. Regarding the electron transfer from the M^0 core to NO_2^-, two mechanisms have been proposed. The first proposed mechanism involves the direct electron transfer from the M^0 core to the NO_2^-, whereas the second mechanism involves indirect electron transfer via H_2 gas produced according to Eq. 6. However, there is still controversy about the dominant electron transfer process.

$$M^0 + 2H^+ \rightarrow M^{2+} + H_2 \uparrow \quad (6)$$

Considering that NO_2^- is a strong oxidant and that surface-bound M^{2+} was often referred to as a stronger reductant, it is suspected that much of these M^{2+} was not accessible by nitrite in the case of Fe and ZnO NP. That is, a more passive oxide coating of varying thickness may always cover the solid/liquid interface and insulate NO_2^- from contacting the active metallic sites. Hence, lower adsorption efficiencies were observed in the case of Fe and ZnO NP when compared to Ag NP (Fig. 4). Moreover, the adsorption of nitrite on ZnO NP follows pseudo second-order kinetic and hence chemisorptions may occur in this case in terms of adsorbate electron affinity as well as local electrostatic attractions between the surface and adsorbate. Chemisorption on oxide surfaces is in many ways markedly different from chemisorption on metals. Oxide surfaces tend to exhibit acid/base or electron donor/acceptor interactions with adsorbates (Miletic et al. 2003).

In each nitrite adsorption/reduction experiment described here, nitrogen and ammonium are the only two products after complete adsorption. At low pH, as in the present investigation, the nitrogen is the desired product, whereas ammonium is the undesired one.

Conclusions

In the medium-term, the removal of nitrite from drinking water is necessary in order to protect the environment and human health. In this work, Ag, Fe and ZnO NP prepared by EEW technique were effective adsorbents for the removal of nitrite from water with very high adsorption capacities at equilibrium. The suitability of the kinetic models for the adsorption of nitrite on the nanoparticles was investigated. Adsorption kinetic data were analyzed using the pseudo first-order, pseudo second-order and intraparticle diffusion model. Ag, Fe and ZnO NP have adsorption properties due to their novel structure, high surface area and high sorption capacities.

ACKNOWLEDGMENT

This research was supported by the Yemeni Ministry of Higher Education & Scientific Research (President of the Republic' Award). The authors thank the technicians of the Chemistry Department, Ibb University for their cooperative help.

REFERENCES

Afkhami, A., and A. A. Mogharnesband. "Kinetic-Spectrophotometric Determination of Trace Amounts of Nitrite by the Reaction of Methyl Orange Formation." Journal of Science, Islamic Republic of Iran 8 (1997): 96-99.

Alqudami, Abdullah, N. A. Alhemiary, and S. Munassar. "Removal of Pb(II) and Cd(II) Ions from Water by Fe and Ag Nanoparticles Prepared using Electro-Exploding Wire Technique." Environmental Science and Pollution Research 19 (2011): 2832-2841.

Alqudami, Abdullah, and S. Annapoorni. "Fluorescent Silver Nanoparticles via Exploding Wire Technique." Pramana–Jouranl of Physics 65 (2005): 815-819.

Alqudami, Abdullah, and S. Annapoorni. "Fluorescence from Metallic Silver and Iron Nanoparticles Prepared by Exploding Wire Technique." Plasmonics 2 (2007): 5-13.

Alqudami, Abdullah, S. Annapoorni, Govind, and S. M. Shivaprasad. "Ag–Au Alloy Nanoparticles Prepared by Electro-Exploding Wire Technique." Journal of Nanoparticle Research 10 (2008): 1027-1036.

Alqudami, Abdullah, S. Annapoorni, S. Lamba, P. C. Kothari, and R. K. Kotnala. "Magnetic Properties of Iron Nanoparticles Prepared by Exploding Wire Technique." Journal of Nanoscience and Nanotechology 7 (2007): 1898-1903.

Aydin, A., O. Ercan, and S. Tascioglu. "A Novel Method for the Spectrophotometric Determination of Nitrite in Water." Talanta 66 (2005): 1181-1186.

Bhattacharyya, K. G., and A. Sharma. "Azadirachta Indica Leaf Powder as an Effective Biosorbent for Dyes: A Case Study with Aqueous Congo Red Solutions." Journal of Environmental Management 71 (2004): 217-229.

Council Directive. 91/676/EEC, Official Journal L 375 (Dec. 1991): 0001-0008.

Davis, A. P. "Field Performance of Bioretention: Water Quality." Environmental Engineering Science 24 (2007): 1048-1064.

Dus, R., and E. Nowicka. "Atomic Deuterium (Hydrogen) Adsorption on Thin Silver Films." Progress in Surface Science 74 (2003): 39-56.

EPA (Environmental Protection Agency). "National Primary Drinking Water Standards (EPA-816-F-03-016)." Office of Water, Washington, DC, June 2003.

Gavagnin, R., L. Biasetto, F. Pinna, and G. Strukul. "Nitrate Removal in Drinking Water: the Effect of Tin Oxides in the Catalytic Hydrogenation of Nitrate by Pd/SnO_2 Catalysts." Applied Catalysis B: Environmental 38 (2002): 91-99.

Ho, Y. S. "Citation Review of Lagergren Kinetic Rate Equation on Adsorption Reaction." Scientometrics 59 (2004): 171-177.

Ho, Y. S., G. McKay, D. A. J. Wase, and C. F. Foster. "Study of the Sorption of Divalent Metal Ions onto Peat." Adsorption Science and Technology 18 (2000): 639-650.

Horold, S., K. D. Vorlop, T. Tacke, and M. Sell. "Development of Catalysts for a Selective Nitrate and Nitrite Removal from Drinking Water." Catalysis Today 17 (1993): 21-30.

Kapoor, A., and T. Viraraghavan. "Nitrate Removal From Drinking Water-Review." Journal of Environmental Engineering - ASCE 123 (1997): 371-380.

Kavitha, D., and C. Namasivayam. "Experimental and Kinetic Studies on Methylene Blue Adsorption by Coir Pith Carbon." Bioresource Technology 98 (2007): 14-21.

Kim, H. H., E. A. Seagren, and A. P. Davis. "Engineered Bioretention for Removal of Nitrate from Stormwater Runoff." Water Environment Research 75 (2003): 355-367.

Lagergren S. "About the Theory of so Called Adsorption of Soluble Substances." K. Sven. Vetenskapsakad. Handl. 24 (1898): 1-39.

Lee, C. K., K. S. Low, and L. C. Chung. "Removal of Some Organic Dyes by Hexane-Extracted Spent Bleaching Earth." Journal of Chemical Technology and Biotechnology 69 (1997): 93-99.

Liou, Y. H., S.-L. Lo, Chin-J. Lin, W. H. Kuan, and S. Chi Weng. "Chemical Reduction of an Unbuffered Nitrate Solution using Catalyzed and Uncatalyzed Nanoscale Iron Particles." Journal of Hazardous Materials 127 (2005): 102-110.

Maroto, Rodríguez- J. M., F. García-Herruzo, A. García-Rubio, C. Gómez-Lahoz, and C. Vereda-Alonso. "Kinetics of the Chemical Reduction of Nitrate by Zero-Valent Iron." Chemosphere 74 (2009): 804-809.

Miletic, M., J. L. Gland, K. C. Hass, and W. F. Schneider. "Characterization of Adsorption Trends of NO_2, Nitrite, and Nitrate on MgO Terraces." Surface Science 546 (2003): 75-86.

Nagaraja, P., J. S. Prakash, and B. L. Bhaskara. "Rapid Spectrophotometric Determination of Trace Amounts of Nitrate-Nitrogen using Dapsone and A-Naphthol." E-Journal of Chemistry 3 (2006): 146-153.

Ozcan, A., A. S. Ozcan, and O. Gok. "Adsorption Kinetics and Isotherms of Anionic Dye of Reactive Blue 19 from Aqueous Solutions onto DTMA-Sepiolite." in: A. A. Lewinsky. (Ed.) "Hazardous Materials and Wastewater-Treatment, Removal and Analysis." Nova Science Publishers, New York, 2007.

Sen, Prasenjit, J. Ghosh, A. Alqudami, P. Kumar, and Vandana. "Novel Process and Apparatus for Producing Metal Nanoparticles." Indian Patent. 840/Del/03, 2003; PCT/IN2004/000067, 2004; International Publication. no WO 2004/112997; World Intellectual Property Organization (WIPO), Paris, 2004; US Patent. Appl. no 20070101823, 2007.

Shuval, H. I., and N. Gruener. "Infant Methemoglobinemia and other Health Effects of Nitrates in Dinking Water." Progress in Water Technology 8 (1977): 183-193.

Singh, N. K., A. Alqudami, and S. Annapoorni. "ZnO Nanoparticles Prepared by an Electroexploding Wire

Technique." Physics Status Solidi A 207 (2010): 2153-2158.

Suzuki, T., M. Moribe, Y. Oyama, and M. Niinae. "Mechanism of Nitrate Reduction by Zero-Valent Iron: Equilibrium and Kinetics Studies." Chemical Engineering Journal 183 (2012): 271-277.

Unuabonah, E. I., K. O. Adebowale, and B. I. Olu-Owolabi. "Kinetic and Thermodynamic Studies of the Adsorption of Lead (II) Ions onto Phosphate-Modified Kaolinite Clay." Journal of Hazardous Materials 144 (2007): 386-395.

Wang, Y., J. Qu, R. Wu, and P. Lei. "The Electrocatalytic Reduction of Nitrate in Water on Pd/Sn-Modified Activated Carbon Fiber Electrode." Water Research 40 (2006): 1224-1232.

Wu, F. C., R. L. Tseng, and R. S. Juang. "Initial Behavior of Intraparticle Diffusion Model used in the Description of Adsorption Kinetics." Chemical Engineering Journal 153 (2009): 1-8.

Abdullah Alqudami was born in Hajjah, Yemen in 1976. In 1999 he graduated with honors from Physics Department of Sana'a University, Yemen. In 1999, he was appointed as junior academic staff at the Physics Department of Ibb University, Yemen and he got dual MSc scholarships granted by Indian Council for Cultural Relations (ICCR) and Ibb University to pursue MSc study at Jawaharlal Nehru University, New Delhi, India. In 2003, he received the M.Sc. degree in Physics from JNU. He was granted a PhD scholarship from Ibb University and he joined the Lab of Professor S. Annapoorni of the Department of Physics & Astrophysics, University of Delhi, India, for four years of research in nanomaterials and he received the Ph.D. degree in November 2007. In January 2008, he joined back Ibb University, Yemen, and he have been appointed as an Assistant Professor of Nano Materials at the Physics Department. In September 2008, he was appointed as the Head of the Physics Department and remained so until September 2012.

As a researcher, he was awarded the President of the Republic of Yemen Award for the promotion of scientific research, first period 2009 for his project on water pollution treatment using metal nanoparticles. He has a good and well known research records in International Journals with good impact factors and good citations. His current and ongoing research includes the preparations, characterizations, and applications of metal and metal oxide nanoparticles. He is trying to control the preparation of such nanoparticles using electro-exploding wire technique, investigate their optical properties, use them for environmental applications such as water treatment, antibacterial, UV blocking, etc., and to explore their toxicity to animals and their biological effects.

Dr. Alqudami is a member of some local and international societies, a referee/reviewer for some international journals in the field of nanoscience and nanomaterials, a member of the editorial board of the International Journal of Materials Science, a member of the Scientific and Technical Committees & Editorial Review Boards of the World Academy of Science, a full member of the American Nano Society, and an Associate Member of the Institute of Nanotechnology, UK.